KEK-TH-1615
Preprint typeset using LaTeX style emulateapj v. 5/2/11

arXiv:1304.0163v2 [astro-ph.HE] 2 Apr 2013

OPENING ANGLE OF COLLAPSAR JETS

Akira Mizuta
KEK Theory Center, Tsukuba 305-0801, Japan

Kunihito Ioka
KEK Theory Center, Tsukuba 305-0801, Japan and
The Graduate University for Advanced Studies (Sokendai), Tsukuba 305-0801, Japan
KEK-TH-1615

ABSTRACT

We investigate the jet propagation and breakout from the stellar progenitor for gamma-ray burst (GRB) collapsars by performing 2D relativistic hydrodynamic simulations with analytical analyses. We find that the jet opening angle is given by $\theta_j \sim 1/5\Gamma_0$, and infer the initial Lorentz factor of the jet at the central engine Γ_0 about a few for observations. The jet keeps the Lorentz factor inside the star by converging cylindrically via collimation shocks under the cocoon pressure, and makes a jet-breakout acceleration before the free expansion to a hollow-cone structure with a sharp edge. Some bursts violating the maximum opening angle $\theta_{j,\max} \sim 1/5 \sim 12°$ imply a two-component jet. We explain both the Amati and Yonetoku spectral relations only with one assumption in the off-center photosphere model. We also numerically calibrate the pre-breakout model (Bromberg et al. 2011) for later use.

Subject headings: gamma rays: bursts — gamma rays: theory — relativity

1. INTRODUCTION

Gamma-Ray Burst (GRB) is the brightest object in the universe. The observed isotropic energy (the apparent energy if it is emitted isotropically) is of the order of or even sometimes more than a solar rest mass energy $M_\odot c^2 \sim 2 \times 10^{54}$ ergs. Current understanding is that the GRB prompt emission is produced by a relativistic collimated jet, whose (half) opening angle is $\theta_j \sim 0.1$ and Lorentz factor is more than $\Gamma > 100$, significantly alleviating the energy requirements.

The opening angle of a GRB jet is an important quantity not only for the energetics but also for the event rate of the GRB. The opening angle also carries information of the central engine. It is difficult to get any information on the opening angle from an observation of the prompt emission, which is beamed into an angle $\sim 1/\Gamma$ by a relativistic effect. The opening angle of a GRB is measured by the light curve of the afterglow that follows the prompt GRB. The afterglow light curve exhibits a break when the jet decelerates to a Lorentz factor of $\Gamma \sim 1/\theta_j$, so-called a jet break, and we can estimate the opening angle from the jet break time (Sari et al. 1999). Recent observations suggest that the opening angle of long GRBs are distributed in several to tens of degrees (6 degrees $\approx$ 0.1 radian) (e.g., Fong et al. 2012).

What physics determines the opening angle of the GRB jet is not known yet. In order to understand the physical origin of the jet opening angle, we have to closely look into the jet propagation and breakout from the surrounding matter. Because some GRBs are associated with supernovae (Galama et al. 1998; Iwamoto et al. 1998; Stanek et al. 2003; Campana et al. 2006; Mazzali et al. 2006), a long GRB is thought to arise from a death of a massive star. A jet is launched deep inside the progenitor, and should break out from the stellar envelope to be observed as a GRB. This is so-called a collapsar model (Woosley 1993; MacFadyen & Woosley 1999). When the jet collides with the stellar envelope, a shocked jet and a shocked envelope move sideways from the jet head and form a cocoon.[1] At the expense of the shocked matter, the jet head moves outward and finally drills a hole in the stellar envelope. This is called the jet breakout.[2]

There are many simulations of the jet propagation for the collapsar model. Aloy et al. (2000) firstly show that a relativistic jet can penetrate the stellar envelope with keeping a good collimation. Zhang et al. (2003, 2004) and Mizuta et al. (2006) study the jet propagation for collapsars with a wide range of jet parameters, such as the luminosity, the initial Lorentz factor and so on. Morsony et al. (2007) discuss the evolution of the jet opening angle and indicate that the opening angle of the jet is relatively smaller than the initial opening angle. However the physical origin of the jet opening angle is still unclear. What determines the opening angle of the jet?

One would consider that the opening angle is given by

$$\theta_j \sim \frac{1}{\Gamma}, \tag{1}$$

where Γ is the Lorentz factor at the jet breakout from the stellar envelope (Matzner 2003; Toma et al. 2007). In order to infer Γ, the cocoon pressure is important as it confines the jet (Matzner 2003; Toma et al. 2007; Ioka et al. 2011). After passing through the collimation shock (Komissarov & Falle 1997), the jet becomes cylindrical since the cocoon pressure is uniform inside the star. A cylindrical jet is actually observed in simulations (Zhang et al. 2003, 2004; Mizuta et al. 2006; Morsony et al. 2007; Lazzati et al. 2009, 2013; Mizuta et al. 2011) and recently discussed by Bromberg et al. (2011) in an analytic way. The Lorentz factor of a cylindrical (stationary) jet is constant $\Gamma \sim \Gamma_0$ because of the flux conservation. Therefore a naive expectation is that the opening angle is given by the inverse of the initial Lorentz factor,

---

[1] In some articles, a cocoon indicates only the shocked jet which has moved sideway. However, the shocked jet is mixed with the shocked stellar envelope by the shear interaction and loses its identity. Since it is difficult to define the contact discontinuity, we use a "cocoon" for both the shocked jet and the shocked stellar envelope in a broad sense.

[2] To be precise, a jet breakout is different from a shock breakout that occurs when a forward shock reaches the stellar surface. This is also different from a jet break seen in the afterglow light curve.

$$\theta_j \sim \frac{1}{\Gamma_0}, \tag{2}$$

as shown in the right panel of Fig. 1 (conventional picture).

In this paper, we explore the evolution of the opening angle for the long GRB jet, and show that the naive expectation in Eq. (2) is partly false. We perform a series of numerical hydrodynamic simulations for jet propagation and breakout from collapsars. We find that the opening angle is a factor ~ 5 smaller than $1/\Gamma_0$, and identify its physical origin with the jet-breakout acceleration, that is, the jet accelerates at the jet breakout before a free expansion as shown in the left panel of Fig. 1 (new picture). The jet-breakout acceleration boosts the Lorentz factor Γ by a factor of ~ 5 larger than Γ_0. Thus Eq. (1) is correct but Eq. (2) is not correct.

We also examine the jet dynamics in an analytical way. We first compare the numerical results with analytic formulae before the jet breakout by Bromberg et al. (2011). Calibrating the model parameters with careful numerical calculations, we make the formulae easier to use. Then we make analytical analyses for the jet-breakout acceleration after the jet breakout.

We further discuss implications of our results. We infer the initial Lorentz factor of the jet ejected from the central engine by using the observed opening angles. We also argue a possible origin of the observed spectral relations, the Amati and Yonetoku relations (Amati et al. 2002; Yonetoku et al. 2004). We derive both the relations with only one assumption $L_j \propto \Gamma_0$, that the total jet luminosity is proportional to the initial Lorentz factor, under the photosphere model of the GRB prompt emission. These are interesting suggestions for the emission mechanism of the prompt emission as well as the jet formation mechanism.

The paper is organized as follows. In Sec. 2, we describe the numerical method and the initial conditions for the jet parameters. We also introduce the probe particles to follow the jet opening angle. In Sec. 3, we show the main results of the hydrodynamic calculations and the time evolution of the opening angles. In Sec. 4, we present the analytic model of the jet dynamics and the opening angle of the jet, and compare it with the numerical results. In Sec. 5, we apply our results with the observations of the opening angle and the spectral relations to probe the initial conditions of the jet from the central engine and the emission mechanism of the prompt emission. Finally, we summarize our results and give conclusions of this work in Sec. 6.

2. NUMERICAL METHOD

2.1. *Numerical scheme*

We have performed two dimensional axi-symmetric relativistic hydrodynamic simulations of jet propagation before and after the eruption from a progenitor surface in order to obtain the final opening angle of the jet θ_j. An updated version of the relativistic hydrodynamic code developed by one of the authors (AM) is used for the hydrodynamic simulations. The code solves special relativistic hydrodynamic equations. We adopt an adiabatic equation of state, $P = (\gamma - 1)\rho\epsilon$, with a constant specific heat ratio, $\gamma = 4/3$, where P is the pressure, ρ is the rest mass density, and ϵ is the specific internal energy.

The hydrodynamic code employs the Godunov type fluxes, i.e., an approximate Riemann solver. The version of Marquina's flux formula (Donat & Marquina 1996) is used for numerical fluxes. The 2nd order accuracy in space is achieved by MUSCL method (van Leer 1977) and the 2nd order accuracy in time is achieved by the total variation diminishing (TVD) Runge-Kutta method (Shu & Osher 1988). Any radiative processes, such as emission or absorption of photons are not included in the calculations. The details of the code and results of 1D and 2D test calculations are presented in the Appendix of Mizuta et al. (2004, 2006).

2.2. *Grid*

A cylindrical coordinate (z, r) is employed for hydrodynamic simulations (z is the direction of jet propagation). In this study, an axi-symmetry is assumed for simplicity. 6400 (z) × 500 (r) grid points are used. The high resolution grid points are devoted around the cylindrical axis so that the interaction with the stellar envelope is well captured in good accuracy. The fine grid points (10^7 cm $\times$ 10^7 cm) are spaced uniformly at $10^9\text{cm} \le z \le 4 \times 10^{10}$ cm and $0 \le r \le 2 \times 10^9$ cm which covers the jet and cocoon at the jet breakout time. Logarithmic linear grids are spaced both in z and r coordinates at 4×10^{10} cm $\le z \le 4.3 \times 10^{11}$ cm and 2×10^9 cm $\le r \le 1.1 \times 10^{11}$ cm. At the outer boundaries, the grid sizes are $\Delta z = 7 \times 10^8$ cm and $\Delta r = 1.6 \times 10^9$ cm, respectively.

We perform a resolution study with twice better resolution of the grids [9728 (z) × 500 (r)]. The fine grid points (5×10^6 cm $\times 5 \times 10^6$ cm) are spaced uniformly at $10^9\text{cm} \le z \le 4 \times 10^{10}$ cm and $0 \le r \le 10^9$ cm which covers the jet and some parts of the cocoon at the jet breakout time. Logarithmic linear grids are spaced both in z and r coordinate at 4×10^{10} cm $\le z \le 6.2 \times 10^{11}$ cm and 1×10^9 cm $\le r \le 1.1 \times 10^{11}$ cm. At the outer boundaries, the grid sizes are $\Delta z = 2 \times 10^9$ cm and $\Delta r = 2.2 \times 10^9$ cm, respectively. The results of the resolution study are given in Sec. 3.7.

The resolution with $\Delta z_{\min} = \Delta r_{\min} = 10^7$cm is comparable with the highest resolution zone in Morsony et al. (2007) who adopted the AMR technique, while our high resolution area covers much larger area. Our resolution study uses $\Delta z_{\min} = \Delta r_{\min} = 5 \times 10^6$cm, which is one of the highest resolutions so far.

The boundary condition is the free boundary condition except for the jet injection region and the cylindrical axis. The reflective boundary condition is imposed at the cylindrical axis.

2.3. *Stellar model*

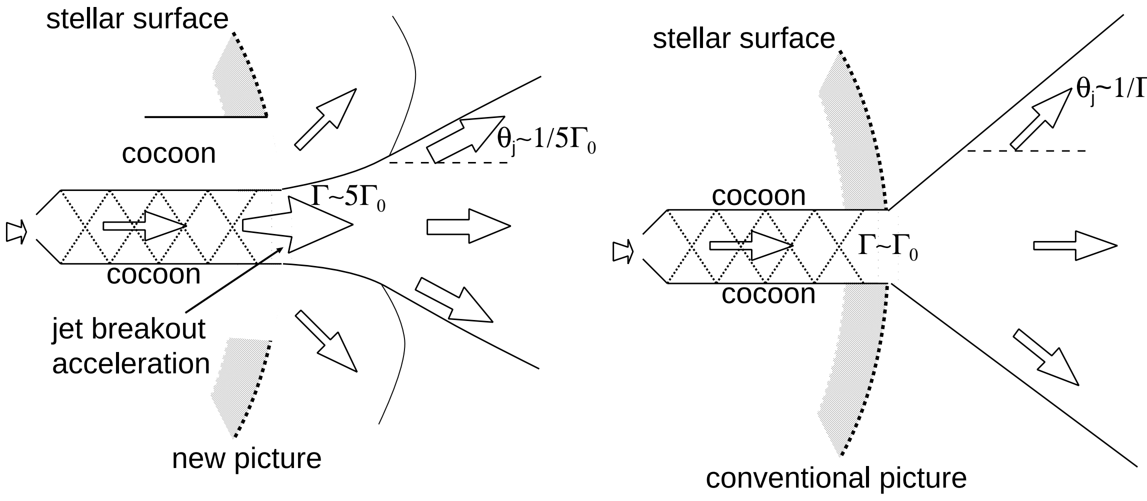

FIG. 1.— Physical pictures of the jet evolution at the jet breakout. Inside the star, the Lorentz factor of the jet keeps the initial value $\sim \Gamma_0$ since the jet is almost cylindrical before the jet breakout. After the jet breakout, the opening angle of the jet is $\sim 1/5\Gamma_0$ (left panel) rather than $\sim 1/\Gamma_0$ (right panel), because the jet-breakout acceleration occurs at the jet breakout where the pressure of the cocoon decreases outward.

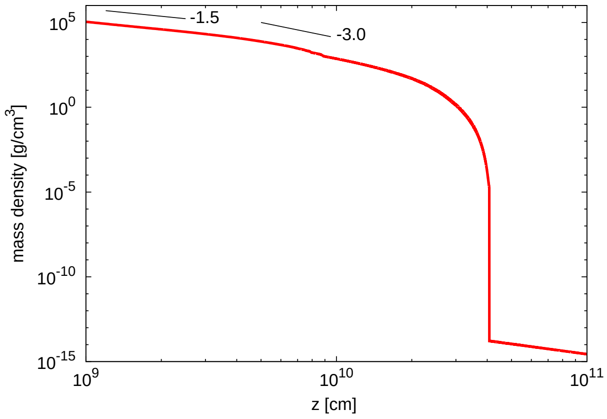

FIG. 2.— Initial radial mass density profile (model 16TI in Woosley & Heger (2006)). The radial mass density profile is almost power law at 10^9cm $\le R \lesssim 6\times 10^{10}$ cm with the index ~ -1.5. Then it quickly drops at $R > 6\times 10^9$ cm. We extend the gas to the outside of the progenitor ($R > 4\times 10^{10}$ cm) which is assumed to be very dilute and a stellar wind profile with the power law index -2.

We adopt one of stellar models in Woosley & Heger (2006) for the progenitor of the GRB. The model is named as 16TI. The total mass and radius of the progenitor at the pre-SN stage are 13.95 solar mass and $R_* = 4\times 10^{10}$ cm, respectively, where R is a radius in the spherical coordinate. The mass density at the innermost boundary ($z = 10^9$ cm) is about 10^5 g cm^{-3}. The radial mass density distribution of the progenitor is almost power-law with an index ~ -1.5 at 10^9 cm $\le R \lesssim 6\times 10^9$ cm and quickly drops at $R > 6\times 10^9$ cm. The mass density at the last grid of the progenitor ($R = R_*$) is 1.7×10^{-5} g cm^{-3}. Outside the progenitor we put a low density gas assuming a stellar wind with the power law index -2, i.e., $\rho(R) = 1.7\times 10^{-14}(R/R_*)^{-2}$ g cm^{-3}. See the radial mass density profile in Fig. 2.

2.4. *Jet conditions*

Assuming the jet formation deep inside the progenitor, we start the numerical calculation at the distance of $z_{\rm min} = 10^9$ cm from the center of the progenitor. From the innermost computational boundary we inlet the jet into the computational domain.

At least, four parameters are necessary to characterize the initial condition of the jet. We choose the cylindrical radius (r_0), the luminosity (L_j), the Lorentz factor (Γ_0), and the specific enthalpy ($h_0 \equiv 1 + \epsilon_0/c^2 + P_0/\rho_0$) of the initial jet, where subscription '0' stands for the injection parameter. Since we inlet the jet parallel to the jet axis with a small radius (r_0), we are not necessary to assume the initial opening angle of the jet (θ_0), which is determined by a relativistic beaming effect as $\theta_0 \approx 1/\Gamma_0$. This allows us to reduce the number of the initial parameters.

(1) We adopt the initial cylindrical radius of the jet as $r_0 = 8\times 10^7$ cm. This value should be sufficiently smaller than Eq. (26) which is supposed to be the cylindrical radius of the jet after the collimation shock (i.e., the cylindrical radius of the jet balanced with the cocoon pressure). If the initial cylindrical radius were larger than Eq. (26), the jet dynamics would be different from the true one because a thick jet sweeps large mass. Even though r_0 should be small, we still need to cover the jet with sufficient grid points. In our simulations, 8 and 16 grid points cover the jet at the boundary for the resolutions, $\Delta z_{\rm min} = \Delta r_{\rm min} = 10^7$ cm and $\Delta z_{\rm min} = \Delta r_{\rm min} = 5\times 10^6$ cm, respectively. Our resolution is high enough to resolve internal structures, such as shocks and vortices, inside the jet and the cocoon.

(2) We consider a constant luminosity jet ($L_j = 5\times 10^{50}$ erg s^{-1}) for simplicity. Thus the explosion energy is $\sim 10^{52}$ ergs for a few tens seconds duration of the jet injection, which is comparable with the values inferred by the observations.

(3) Another two parameters to define the initial jet are the specific enthalpy (h_0) and the Lorentz factor of the jet (Γ_0). We fix the product of two parameters, i.e., $h_0\Gamma_0$ to be 538 in this paper. The product $h_0\Gamma_0$ gives the maximum Lorentz factor achieved by the adiabatic expansion, since $h\Gamma$ is conserved by the relativistic Bernoulli's principle along a stream line for a steady state. A gas with

large enthalpy ($h \gg 1$) expands adiabatically by decreasing h and increasing Γ, i.e., the jet accelerates with fixing $h\Gamma$. Our assumption ($h_0\Gamma_0 = 538$) satisfies $h_0\Gamma_0 > 100$ which is required for avoiding the compactness problem of the GRB. The recent Fermi bursts suggest a relatively large $h\Gamma$ (Abdo et al. 2009; Ackermann et al. 2010; Ioka 2010).

(4) The initial Lorentz factors, $\Gamma_0 = 2.5$, 5, and 10, are studied to see the dependence on Γ_0 for the jet dynamics and the opening angle after the jet breakout. These are the models, G2.5 ($\Gamma_0 = 2.5$), G5.0 ($\Gamma_0 = 5$), and G10 ($\Gamma_0 = 10$), respectively. We also perform the hydrodynamic simulations with higher resolutions. These are the models, G2.5H ($\Gamma_0 = 2.5$), G5.0H ($\Gamma_0 = 5$), and G10H ($\Gamma_0 = 10$), respectively. Since we fix $h_0\Gamma_0 (= 538)$, the initial enthalpy (h_0) is the smallest ($h_0 = 53.8$) for the case with $\Gamma_0 = 10$. Thus all jets are initially thermal-dominated plasma ($h_0 \gg 1$). The initial specific internal energy (ϵ_0/c^2) is 80 for the model with $\Gamma_0 = 5$. As shown later, these initial Lorentz factors are crucial parameters for the final opening angles. We set the velocity vector of the jet initially parallel to the z-axis. The jet expands with an initial opening angle $\sim 1/\Gamma_0$ as long as the injection angle is less than $\sim 1/\Gamma_0$.

Table 1 summarizes the jet initial conditions of our models.

2.5. *Probe particles*

In order to follow the Lagrange motion of the fluid elements, we introduce probe particles to trace the path of the fluid elements. It is necessary to follow the Lagrange motion of the fluid elements to define the opening angle of the jet, since the jet opening angle depends on the time. Every 0.01 s, 32 particles are injected into the computational domain with the jet. At the injection region at $z_{\rm min} = 10^9$ cm, 32 particles are uniformly spaced at $0 \le r \le r_0 = 8 \times 10^7$ cm. In every hydrodynamic time steps (Δt), the particles move with their local velocities calculated by the hydrodynamic simulation, i.e, $\boldsymbol{x}_{\rm new} = \boldsymbol{x}_{\rm old} + \boldsymbol{v}\Delta t$, where $\boldsymbol{x}$ is the position of a particle and $\boldsymbol{v}$ is the local velocity.

Tracing the Lagrange motion of the fluid elements allows us to find the location where and how the free expansion starts after the jet breakout. Since we define the jet opening angle by the direction of free expansion (see, Sec.3.4), the information of the Lagrange motion is very important for quantitative analysis, especially to find a relation between the opening angle and Lorentz factor. The particle path is also useful to identify whether the fluid elements have moved into the cocoon or not.

3. RESULTS

3.1. *Overall evolution*

The jets in all models of Table 1 succeed to drill the stellar envelops. Before the jet breakout, the jet hits at the reverse shock that is produced by the interaction between the jet and the stellar envelope. Then the shocked jet moves sideway, forming a high pressure cocoon, as shown in the schematic figure 3. The high pressure in the cocoon works to confine the jet. The jet is confined through a collimation shock which deflects the velocity vector into a parallel direction to the cylindrical axis. The high pressure cocoon is also discussed in the context of FRII jets (Begelman & Cioffi 1989).

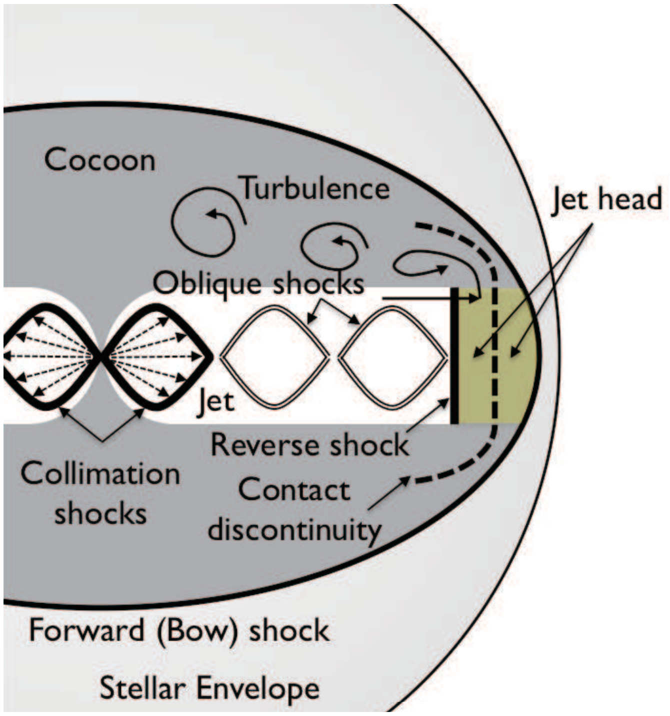

FIG. 3.— A schematic figure of the jet during the forward shock is inside the progenitor star.

When the forward shock reaches the stellar surface, the shocked stellar envelope starts to expand into the circumstellar matter, i.e., a shock breakout. Soon the jet also start to expand into the circumstellar matter, i.e., a jet breakout as presented in previous numerical simulations (Aloy et al. 2000; Zhang et al. 2003, 2004; Mizuta et al. 2006; Morsony et al. 2007; Mizuta & Aloy 2009; Mizuta et al. 2011; Nagakura et al. 2011). After the jet breakout, the jet advances in the circumstellar matter which is assumed to be very dilute.

3.2. *Before the jet breakout*

The jet is well confined by the high pressure cocoon before the jet breakout. Figure 4 shows the contours of the mass density, the pressure and the Lorentz factor of the jet just before the jet breakout for the model G5.0 ($\Gamma_0 = 5$). We should note that the r axis is elongated and the aspect ratio of z and r is not unity in order to highlight the fine structures in the jet and the cocoon. Although we inlet a jet with a velocity parallel to the cylindrical axis, the jet tries to expand with an opening angle of $\theta_0 \sim {\Gamma_0}^{-1}$ because the thermal energy is large. Around the injection point, the Lorentz factor rapidly increases and then drops across a discontinuity. Since the pressure and the mass density increase across this discontinuity, it is the shock surface. The shock deflects the velocity vector almost towards the jet axis, and is so-called the collimation shock. The collimation shock is produced by the interaction between the expanding jet and the high pressure cocoon (Komissarov & Falle 1997, 1998; Bromberg & Levinson 2009; Bromberg et al. 2011). To distinguish it from the other collimating oblique shocks in the jet, we sometimes call it the first collimation shock. See a schematic figure 3.

As shown in Fig. 4, after the first collimation shock,

TABLE 1
Jet initial conditions of the models

model	Γ_0 [a]	luminosity (L_j) (erg s^{-1})	initial jet cylindrical radius (r_0) (cm)	$h_0\Gamma_0(\cong \Gamma_\infty)$	$\Delta z_{\rm min} = \Delta r_{\rm min}$ [b] (cm)
G2.5	2.5	5×10^{50}	8×10^7 cm	538	10^7 [c]
G5.0	5.0				
G10	10				
G2.5H	2.5	5×10^{50}	8×10^7 cm	538	5×10^6 [d]
G5.0H	5.0				
G10H	10				

[a] Initial Lorentz factor
[b] Highest resolution grid size in the computational domain
[c] at the region of 10^9cm $\le z \le 4 \times 10^{10}$ cm and $0 \le r \le 1 \times 10^9$ cm
[d] at the region of 10^9cm $\le z \le 4 \times 10^{10}$ %rmcm and $0 \le r \le 1 \times 10^9$ cm

the jet keeps an overall cylindrical shape (Bromberg et al. 2011). The Lorentz factor increases to a few tens and then drops to $\sim \Gamma_0$, i.e., the initial Lorentz factor, after the first collimation shock, see Eq. (20). We can understand the cylindrical evolution as follows. The propagation velocity of the jet head is comparable to the sound velocity of the shocked envelope (obviously) and is much smaller than the sound velocity of the shocked jet (with high entropy) at the jet head. The shocked jet goes backward around the jet and provides an constant cocoon pressure over the jet. Namely the flow in the cocoon is sub-sonic. Although the mean sound velocity of the cocoon, which is comparable to the transverse velocity of the bow shock, is lower than the jet head velocity, the matter is only partially mixed in the cocoon. Thus the gas in the cocoon can communicate with each other, resulting in a homogeneous pressure profile in the cocoon. Figure 5 shows the pressure profile at $r = 1.8 \times 10^9$cm as a function of z. At $t = 3$ s (before the jet breakout), we can see a relatively constant pressure profile over the cocoon. Since the jet is confined by the homogeneous pressure in the cocoon, the jet keeps a cylindrical structure after passing the first collimation shock. The Lorentz factor should be constant over the cylindrical jet because of the flux conservation. The Lorentz factor keeps $\sim \Gamma_0$, though some fluctuations appear in the Lorentz factor due to the internal oblique shocks.

The internal oblique shocks occur in the cylindrical jet for several reasons. First reason is that the jet is over-deflected to the axis after the first collimation shock. The jet shrinks the cylindrical radius, resulting in an oblique shock. Second reason is similar to that for the first collimation shock. The shrinking jet becomes over-pressured and makes a bounce. This is like the initial expansion at the injection and thereby leads to the second collimation shock. Such a cycle of the expansion and the collimation is repeated several times. Note that the jet has larger initial cylindrical radius in the second and later collimations than in the first one. Third reason is the fluctuation of the cocoon pressure (Mizuta et al. 2004). The cocoon is produced by the the shocked jet and the shocked envelope. The shocked jet at the jet head go sideways and also backward under the pressure of the shocked envelope (Mizuta et al. 2010). Together with the shear motion between the shocked jet and the shocked envelope, a large vortex and a turbulent structure is formed in the cocoon. The turbulence in the cocoon makes a perturbation at the contact discontinuity between the cocoon and the jet, which causes the oblique shocks in the jet. Since shocks are tilted to the jet axis, we call these shocks as oblique shocks in the jet.

At the last stage of the propagation in the progenitor, we identify a jet-breakout acceleration. Since the density distribution of the envelope exponentially drops at the stellar surface R_* ($z = 4 \times 10^{10}$ cm, see Fig. 2), the jet head advances rapidly ($\sim c$, the light speed). As a result the pressure profile in the cocoon can not keep constant around the jet head. The pressure profile in the cocoon drops near the jet head. See the one dimensional pressure profile in the cocoon in Fig. 5 at $t = 4.5$ s when the jet breakout just occurs. The jet can not keep the cylindrical structure near the jet head even after passing the oblique shock, since the cocoon pressure drops before the jet breakout. The jet expands in a decreasing cocoon pressure and makes an acceleration by converting the thermal energy into the kinetic energy. The Lorentz factor of the jet increases to a few tens even after the oblique shock. See the Lorentz factor contour near the jet head in Fig. 4 and the discussions in Sec. 4.2.

3.3. *After the jet breakout*

Soon after the forward shock reaches the stellar surface, the jet breakout occurs. The jet and the cocoon (a mix of the shocked jet and the shocked stellar envelope) start to expand into the circumstellar matter which is assumed to be very dilute. The expansion velocity of the cocoon is comparable to the sound velocity before the jet breakout ($\sim$ a few tens percents of the light speed). So the cocoon stays near the stellar surface for ten seconds, providing a pressure for the jet confinement. As shown in Fig. 5 for $t = 5.2$ s, the cocoon pressure is decreasing outward, ranging from $P \sim$ const to $P \propto z^{-4}$.

On the other hand, the supersonic jet does not notice the cocoon profile until a collimation shock is formed. In the star, the jet is repeating a cycle of the expansion and the (over-)collimation (see Sec. 3.2 and 3.4), and a certain expansion starts in the outward-decreasing pressure. Note that the expansion is off-center near the stellar surface, not from the stellar center. The off-center origin makes the pressure profile shallower than that shown in Fig. 5 with the stellar center origin. Since the pressure profile is still shallower than $P \propto z^{-2}$, the jet is collimated but the collimation is not enough to keep the cylindrical radius (see Sec. 3.4). This expansion leads to the jet-breakout acceleration, as shown in Sec. 4.2. Even after the last collimating oblique shock, a certain level of confinement continues without forming a shock (or with a weak shock), but the jet makes an expansion, leading

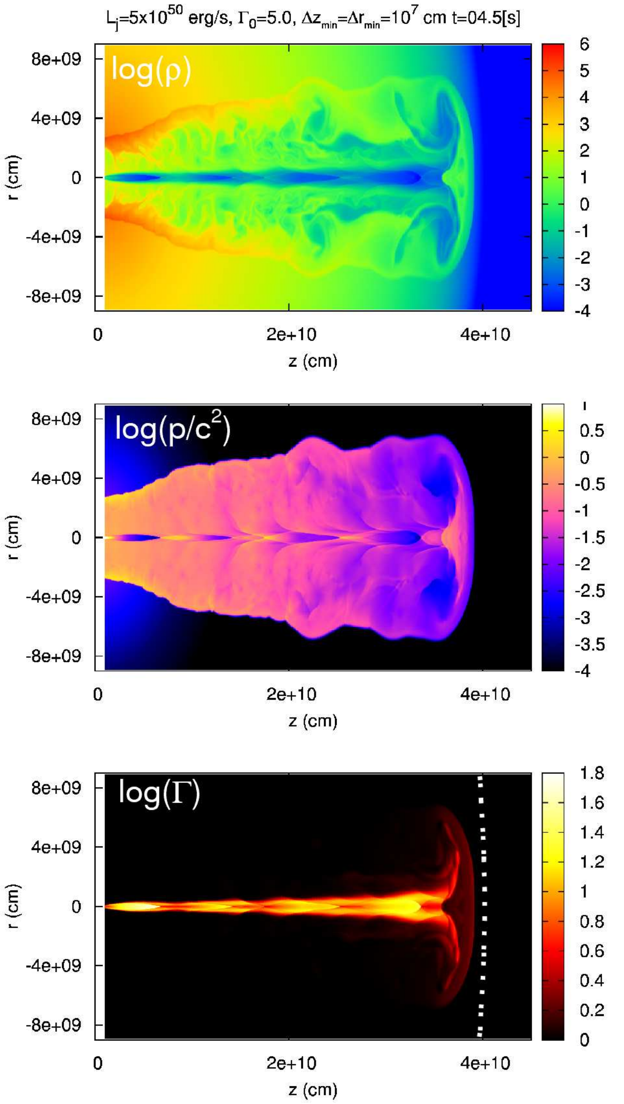

FIG. 4.— Mass density in g cm^{-3} (top), pressure in dyn cm$^{-2}/c^2$ (middle), and Lorentz factor (bottom) contours of the model $\Gamma_0 = 5$ at $t = 4.5$ s (model G5.0). Note that the aspect ratio of z and r is not unity in order to enhance the fine structures in the jet and the cocoon. White dashed line in the Lorentz factor contour indicates the initial stellar surface.

to an additional jet-breakout acceleration (see Sec. 4.2). Finally the jet starts to expand freely after the pressure profile gets steeper than $P \propto z^{-4}$. As time goes on, the steep pressure profile moves inward, while the first collimation shock becomes large. Then the jet starts a free expansion after crossing the first collimation shock.

Figure 6 shows the mass density, the pressure, and the Lorentz factor contours of the model G5.0 ($\Gamma_0 = 5$) at $t = 6.4$ s. There are many oblique shocks in the jet, not only inside the progenitor but also outside the progenitor.

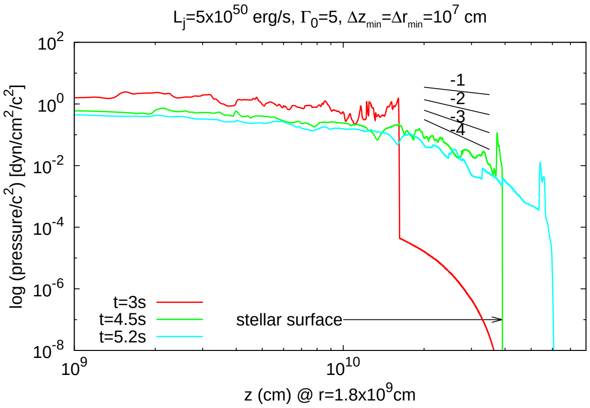

FIG. 5.— One dimensional pressure profiles at $r = 2 \times 10^9$ cm and $t = 3,\ 4.5,\ 5.2$ s for model G5.0. The profile shows the cocoon region. The shocked ambient gas appears as a thin shell at the jet head. The pressure profile is almost homogeneous before the jet breakout ($t = 3$ s). When the jet breakout occurs at $t = 4.5$ s, a pressure gradient can be seen around the jet head. After the jet breakout $t \gtrsim 5.2$ s, the pressure profile in the outer cocoon is about $p \propto z^{-4}$. Note that the profile becomes shallower if the origin is off-center.

The oblique shocks outside the star are imprinted before the free expansion and expanding in a self-similar way, because the internal shocks are not developed in freely accelerating flow without confinement (Ioka et al. 2011). The jet advances with a velocity close to the speed of the light, whereas the cocoon expands with a sub-relativistic speed.

3.4. *Opening angle after the jet breakout*

Since probe particles are introduced in the jet (Sec. 2.5), we can trace the particle path and measure the opening angle of the jet. Figure 7 shows the traces of particles that are injected at the same time ($t = 5$ s). The path of each particle repeats a cycle of an expansion and a collimation inside the star, and the last collimation near the stellar surface is not so strong that the cylindrical radius of the jet becomes large. Just outside the progenitor ($R \gtrsim R_* = 4 \times 10^{10}$ cm), the particles do not yet start a free expansion. At some distances which depends on the particles, the particle path finally becomes straight, i.e., the jet freely expands as discussed in the previous section. The position where the particle path gets straight depends on when and where the particle is injected. The locations to start the free expansion are $\sim 5 \times 10^{10}$ cm for early particles which were near the head of the jet at the jet breakout. Then the locations to start the free expansion move inward for subsequent particles.

Arrows in Fig. 7 indicate the slopes of the inverse of the local Lorentz factor (Γ^{-1}) for the laterally outermost particle. The left arrow is Γ^{-1} just after the last collimating oblique shock ($z \sim 3.3 \times 10^{10}$ cm). Although the jet behind the shock has higher Lorentz factor than that in the star, the arrow is pointing outside the jet opening angle. Thus the jet is still confined by the cocoon and can not expand freely, drawing a concave particle path in Fig. 7. Finally the path becomes straight from the base of the right arrow ($z \sim 5 \times 10^{10}$ cm). The direction

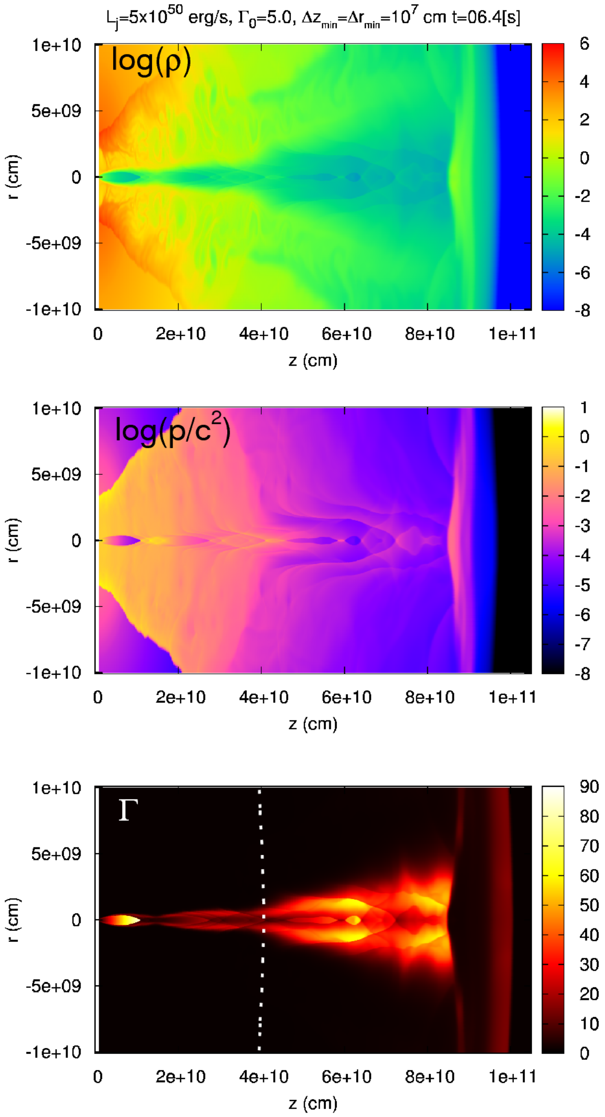

Fig. 6.— Same as Fig. 4 but after the jet breakout (at $t = 6.4$ s, model G5.0).

of the arrow almost coincides with the freely expanding direction. This means that the opening angle of the jet is determined by the Lorentz factor of the flow when the free expansion starts as in Eq. (1).

The extrapolations of the free expansion lines do not cross the center of the progenitor, i.e., the explosion is off-center. The explosion center moves gradually inward as time passes. The off-center position is different even for particles injected at the same time.

Since the particles with $h\Gamma < 100$ lose their potential to reach $\Gamma \geq 100$ by an adiabatic expansion, the only particles with $h\Gamma \geq 100$ contribute to the GRB prompt emission. The baryon loading occurs for the particles once involved in the cocoon component before the free expansion, because the turbulence in the cocoon mixes the shocked jet and the shocked stellar envelope. The baryon loading also occurs at the contact discontinuity between the jet and the cocoon even after the jet breakout (mostly via numerical diffusion). A certain level of baryon loading is unavoidable through the numerical diffusion, and we should be careful about it as discussed in Sec. 3.7. Most particles which are injected in early time exhibit $h\Gamma < 100$ at large z.

We measure the jet opening angle (θ_j) by the angle between the jet axis and the free expansion path for the laterally outermost particle. Figure 8 shows the time evolution of the jet opening angle for each model. The solid lines show the opening angles measured by the particles with $h\Gamma \geq 100$, while the dashed lines have $h\Gamma < 100$ that can not produce GRBs. The time axis in Fig. 8 corresponds to the time when the particles are injected. Since the jet breakout time depends on the models, we align the shock breakout time at $t = 0$ in Fig. 8. Thus the time $t < 0$ indicates that the particles move into the cocoon before the shock breakout.

The opening angle of the jet is not constant in early times as shown in Fig. 8. There are particles with $h\Gamma < 100$ before and a few seconds after the shock breakout. Those particles are the components that are engulfed into the cocoon before the jet breakout. The cocoon is largely baryon-loaded because the shocked envelope mixes with the shocked jet by the shear interaction through the contact discontinuity. Since the particles expand with the cocoon after the shock breakout, those opening angles are relatively large.

The opening angle drops after the shock breakout in Fig. 8. At the same time, the baryon-poor GRB component $h\Gamma \geq 100$ appears. We note that our results are not sensitive to the threshold value of $h\Gamma \geq 100$ because the baryon-loaded flow and the baryon-poor flow are well separated, irrespective of a certain uncertainty in the numerical baryon loading (see also Sec. 3.5). The opening angle settles down to a nearly constant value a few seconds after the shock breakout. Small time variabilities of the opening angle are caused by the fluctuations of the local Lorentz factor just before the free expansion, according to Eq. (1). The local Lorentz factor depends on where and how the particle crosses the collimation shock. Since the size of the first collimation shock grows up to a comparable size of the stellar radius, the later particles only pass the first collimation shock before the free expansion.

Most importantly, the opening angles in Fig. 8 are much smaller than Γ_0^{-1}, contrary to our naive expectations ($1/\Gamma_0 \sim 0.2$ rad for $\Gamma_0 = 5$ and $1/\Gamma_0 \sim 0.1$ rad for $\Gamma_0 = 10$). Figure 9 shows $\theta_j - \Gamma_0^{-1}$ plot for the models. We plot the opening angles at different times (from $t = 3$ s to 7 s) since they fluctuate as shown in Fig. 8. The opening angles of the jet are not on the line $\theta_j \sim \Gamma_0^{-1}$ but on the line $\theta_j \sim (5\Gamma_0)^{-1}$. This is our main results; the opening angle of the GRB jet from collapsars is roughly given by

$$\theta_j \simeq \frac{1}{5\Gamma_0}. \quad (3)$$

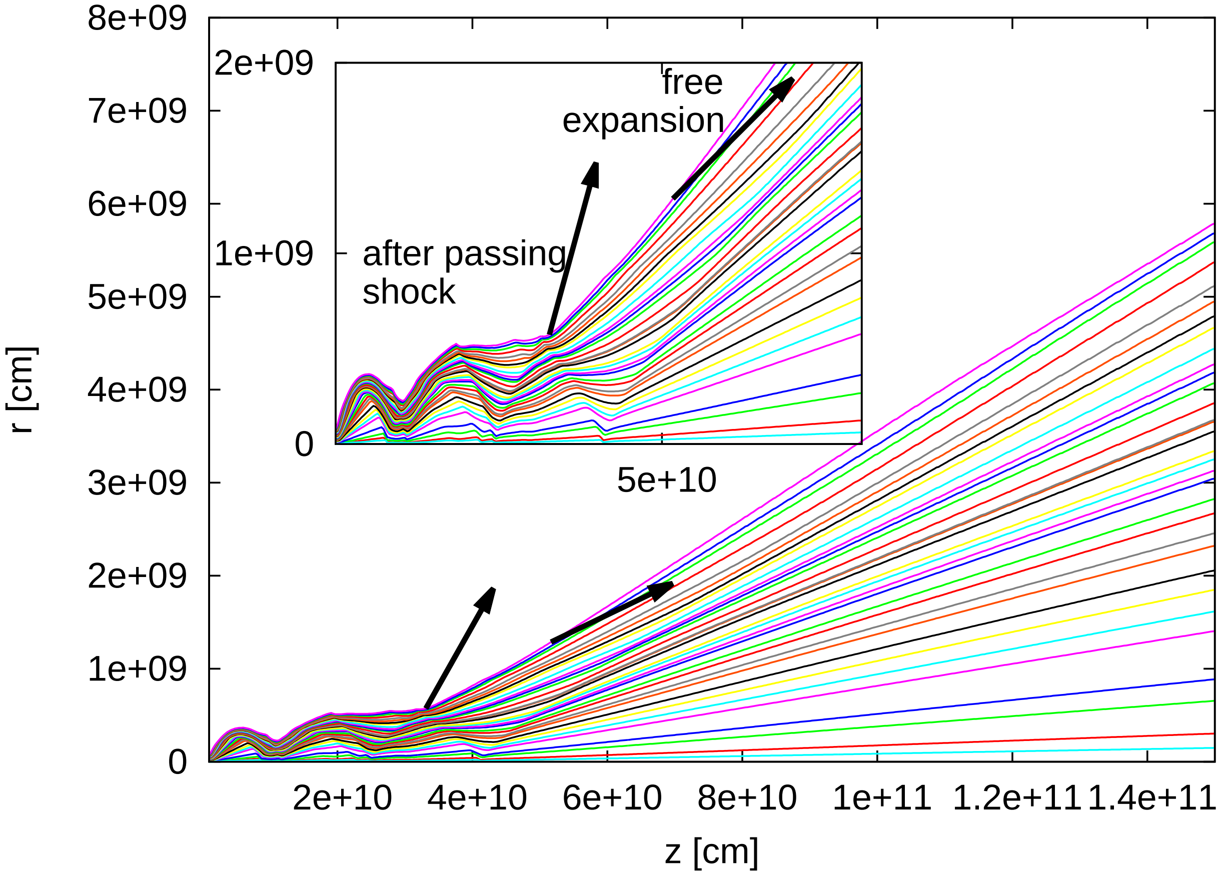

FIG. 7.— Particle trajectories injected with the jet at the same time ($t = 5$ s, model G5.0). The arrows indicate the slope of the inverse of the local Lorentz factor (Γ^{-1}) at the time when the particle has passed the final collimating oblique shock before the free expansion (left arrow) and at the time when the free expansion starts (right arrow) for the laterally outermost particle. The free expansion direction almost coincides with the slope of the inverse of the local Lorentz factor (Γ^{-1}) when the free expansion starts. The inset displays a zoom of the range 1×10^9 cm $\leq z \leq 8 \times 10^{10}$ cm. Note the aspect ratio of z and r is not unity.

3.5. *Angular profile of the jet after the jet breakout*

Figure 10 shows the angular distribution of isotropic luminosity ($L_{\rm iso}$) using the hydrodynamic quantities of the fluid calculations without any constrain for $h\Gamma$, at $R_a = 1.5 \times 10^{11}$ cm at the time when the forward shock reaches at $z_{FS} = 3 \times 10^{11}$ cm, for models G2.5 ($t =$ 14.8 s), G5.0 ($t = 12.5$), G10 ($t = 11.9$ s). The angle is in spherical coordinate whose origin is the center of the progenitor. The angular distribution of the isotropic luminosity profile shown in Fig. 10 roughly corresponds to the particles at $t = (z_{FS} - R_a)/c = 5$ s after the shock breakout in Fig. 10. The arrows indicate the opening angle of the jet measured in Fig. 10 for each model. Each arrow roughly coincides with the rim at which the isotropic luminosity starts to drop exponentially. Our results are not sensitive to the threshold value of $h\Gamma \geq$ 100, irrespective of a certain uncertainty in the numerical baryon loading.

Fig. 10 shows a hollow-cone jet structure. The angular distribution of the isotropic luminosity is high at the rim and drops exponentially at the edge. Then it gradually decreases at large angles. The high isotropic luminosity rim part is produced by the shock between the expanding jet and the high density cocoon before the free expansion. The other oblique shocks produced in the star also make the structured jet at large z in Fig. 6 and 10.

Angular distributions of the jet are also shown by Zhang et al. (2004); Morsony et al. (2007); Mizuta & Aloy (2009). Since they take the radial integration of the energy density or the time integration of the energy flux at a certain radius, not a snapshot of the isotropic luminosity, we can not simply compare their results with ours. In fact there are some differences, but it is difficult to identify the reasons such as the numerical diffusion, the initial jet size, and so on.

3.6. $\Gamma_0 = 2.5$ *case*

The behavior of the jet for the case $\Gamma_0 = 2.5$ is somewhat different from other cases ($\Gamma_0 = 5$ and 10). The jet opening angle at the injection point for the model $\Gamma_0 = 2.5$ is larger than those for other models, since

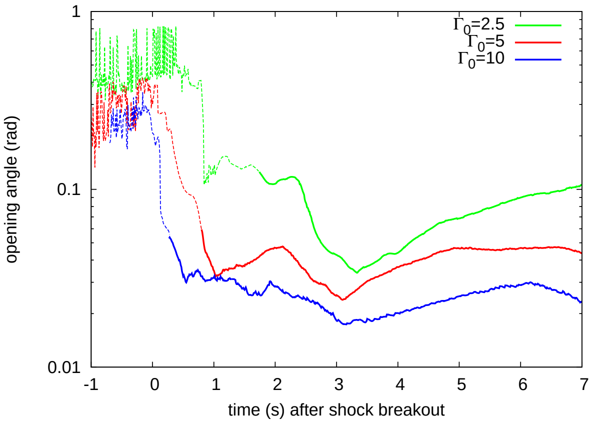

FIG. 8.— Opening angles as a function of time before and after the shock breakout for the resolution $\Delta z_{\min} = \Delta r_{\min} = 10^7$cm cases (models G2.5, G5.0, and G10) are shown. The opening angles are measured by using probe particles (see Sec. 3.4). The components which satisfies $h\Gamma \geq 100$ are indicated by solid lines. Those are components to be accelerated $\Gamma \geq 100$ by the adiabatic expansion and can contribute to the prompt emission. The components with $h\Gamma < 100$ via the baryon loading from the shocked stellar envelopes are shown by the dashed lines.

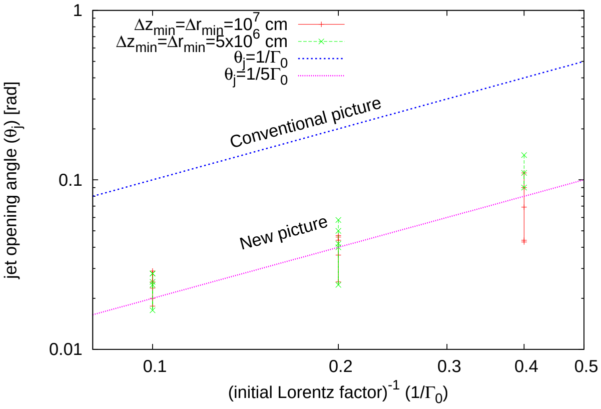

FIG. 9.— Opening angle (θ_j) − inverse of the initial Lorentz factor (Γ_0^{-1}) plot. The opening angles at $t = 3$, 4, 5, 6 and 7 s are shown for models G2.5, G5.0 and G10 with the resolution $\Delta z_{\min} = \Delta r_{\min} = 10^7$ cm. The opening angles are also shown at $t = 3$, 4, 5, 6 and 7 s for models G5.0H and G10H and at $t = 5$, 6, and 7 s for model G2.5H with the resolution $\Delta z_{\min} = \Delta r_{\min} = 5 \times 10^6$ cm. We also plot lines of $\theta_j = \Gamma_0^{-1}$ (conventional picture by naive expectation) and $\theta_j = (5\Gamma_0)^{-1}$ (our new picture obtained by numerical simulations).

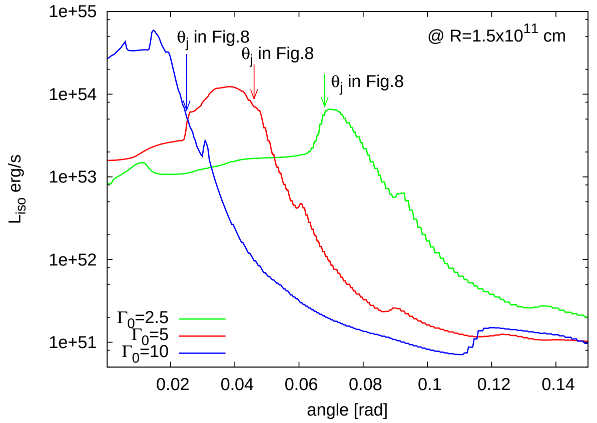

FIG. 10.— Angular energy density distribution after the jet breakout at a spherical radius ($R = 1.5 \times 10^{11}$ cm) for models G2.5 at $t = 14.8$ s (green), G5.0 at $t = 12.5$ (red), and G10 at $t = 11.9$ s (blue). The time is when the forward shock reaches at $z = 3 \times 10^{11}$ cm. The energy density distribution of the jet shows a hollow-cone structure. The jet opening angles at $t = 5$ s in Fig. 8 are indicated by the arrows for each model, and coincides with the position at which the energy density starts to drop exponentially.

the initial opening angle is $\sim \Gamma_0^{-1}$. The cylindrical radius of the jet becomes larger than those of other models (see the analytic study of the jet dynamics in the progenitor in Sec. 4.1). As the cylindrical radius of the jet increases before the jet breakout, the momentum flux per area to push the stellar envelopes decreases, resulting in the strong reverse shock. As a result, the forward shock and the reverse shock go away from each other as shown in Fig 12. The reverse shock is far from the progenitor surface at $z \sim 2.4 \times 10^{10}$ cm at the time when the forward shock reaches the stellar surface, $z \sim 4 \times 10^{10}$ cm. Since the cylindrical radius of the jet is very large, a large fraction of the shocked jet and the shocked envelope can not go sideways and remains in the jet head. The mass is collected at the jet head like a snowplow or a plug (Zhang et al. 2004; Mizuta et al. 2006). Even after the shock breakout, the plug remains on the axis and affects the jet advance for a while. As the plug moves away from the star, the jet can go around the plug more easily and the effect of the plug decreases. A similar structure would also appear for the low luminosity jets with $L_j < 5 \times 10^{50}$ erg s^{-1} (e.g., Toma et al. 2007), while the plug would be reduced for a non-axisymmetric case (Zhang et al. 2004). We will study the luminosity dependence in the near future.

The plug affects the time evolution of the opening angle after the jet breakout. The opening angle in the case of $\Gamma_0 = 2.5$ does not drop quickly, compared with the other models. It takes a few seconds to start to drop and gets much smaller angle than Γ_0^{-1}. As shown in Fig. 12, there is a baryon-rich plug ahead of the jet when the jet breakout occurs. The jet is scattered by the plug for a few seconds after the jet breakout. As a result the opening angle of the jet gets large for a while. When the following jets do not interact with the plug which moves far away from the progenitor, the opening angle gets small as other models.

3.7. *Resolution study*

We have done hydrodynamic simulations with higher resolution as discussed in Sec. 2.2. The initial jet contains a small amount of baryon, while the stellar envelope contains abundant baryons, i.e., $h\Gamma \sim 1$. As the jet proceeds in the stellar envelope, the contact discontinuity is formed between the shocked jet and the shocked stellar envelope. Our numerical calculations use the fixed grid points. Artificial baryon loading could happen when the discontinuity crosses the grids via the nu-

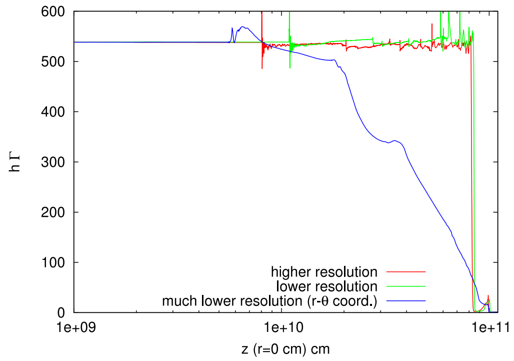

Fig. 11.— One dimensional profile of the Bernoulli's constant $h\Gamma$ along the jet axis for $\Gamma_0 = 5$ at $t = 6.4$ s when the forward shock reaches $z \sim 10^{11}$ cm. Both resolution cases, i.e., $\Delta z_{\rm min} = \Delta r_{\rm min} = 10^7$cm (model G5.0) and $\Delta z_{\rm min} = \Delta r_{\rm min} = 5 \times 10^6$cm (model G5.0H) are shown. $h\Gamma$ is conserved up to the jet head except some fluctuations at the internal shocks. On the other hand, $h\Gamma$ drops near the jet head for a simulation with similar jet parameters but a low-resolution spherical coordinate, $\Delta\theta = 0.25$ degrees, (Mizuta et al. 2011) due to the baryon loading via the interaction with the stellar envelope.

merical diffusion. Once the gas is polluted by baryons ($h\Gamma \sim 1$), it is not accelerated to a large Lorentz factor by the adiabatic expansion. Figure 11 shows one dimensional profile of $h\Gamma$ along the jet axis for $\Gamma_0 = 5$ at $t = 6.4$ s when the forward shock reaches $z \sim 10^{11}$ cm with both resolution cases, i.e., $\Delta z_{\rm min} = \Delta r_{\rm min} = 10^7$cm and $\Delta z_{\rm min} = \Delta r_{\rm min} = 5 \times 10^6$cm. In both cases, the Bernoulli's constant $h\Gamma$ is conserved all the way to the jet head except for some fluctuations at the internal shocks. If we apply poor resolution, the Bernoulli's constant $h\Gamma$ is not well conserved. For example, the case of Mizuta et al. (2011) is also shown. $h\Gamma$ is conserved up to a half of the jet but not near the jet head due to the numerical baryon loading. Mizuta et al. (2011) adopted similar jet parameters but a spherical coordinate for hydrodynamic simulations with $\Delta\theta = 0.25$ degrees around the jet axis. This is one of the reasons to use much higher resolution grid points for detailed quantitative discussions on the opening angle of the jet.

Fig. 9 shows the opening angles for different resolutions. The results are similar between different resolutions. Therefore the relation $\theta_j \sim (5\Gamma_0)^{-1}$ in Eq. (3) seems robust.

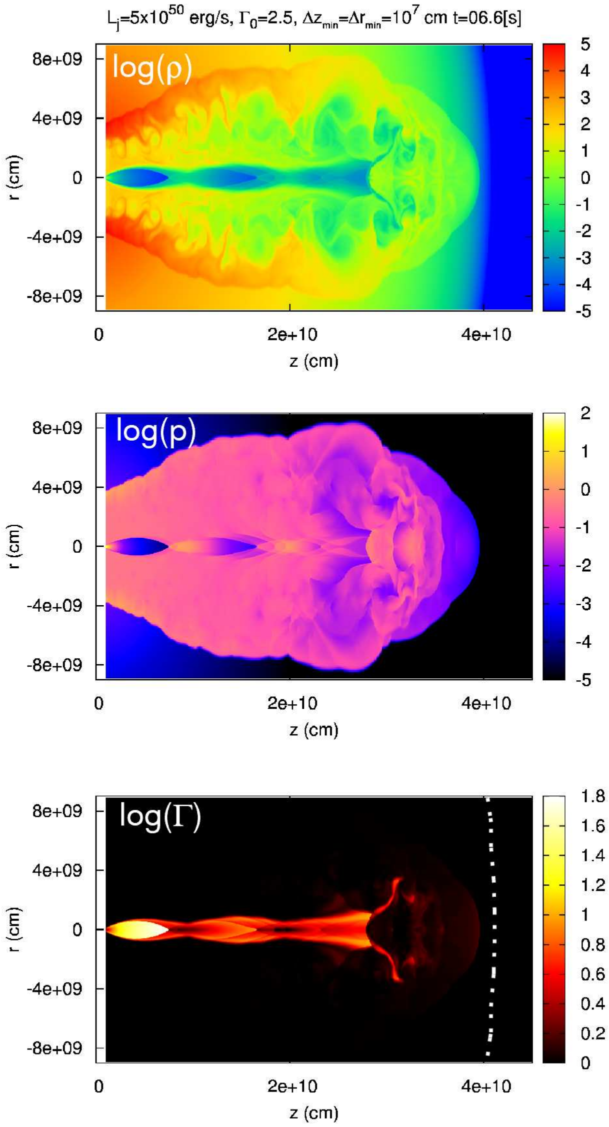

Fig. 12.— Same as Fig. 4 but $\Gamma_0 = 2.5$ (model G2.5), just before the shock breakout ($t = 6.6$ s).

Although the differences are small between the models G2.5 and G2.5H ($\Gamma_0 = 2.5$), they depend on the resolution most sensitively than the other models. Figure 13 shows the mass density, the pressure, and the Lorentz factor contours of the model $\Gamma_0 = 2.5$ with the high resolution at $t = 7.5$ s when the shock breakout occurs. The shock breakout times (6.6 sec and 7.5 sec) are different by ~ 1 sec even if the jet parameters are the same in Fig. 12 and and 13. The high resolution case takes about 1.2 times longer time than the lower resolution case. One can notice that the recollimation shocks are different. The low resolution one converges on the axis while the high resolution one makes a Mach disk. Probably the difference is caused by the nonlinear evolution of the jet and the cocoon dynamics. A small difference in the oblique shocks near the head of the jet changes the cross-sectional radius of the reverse shock and hence the jet head speed. This affects the difference in the appearance of vortices and the turbulence in the cocoon (Mizuta et al. 2010). The turbulence itself is also a nonlinear process. The numerical diffusion of the baryon loading would also alter the dynamics. The size of the head plug is also larger for the high resolution than that for the low resolution when the jet breakout occurs.

3.8. *Initial jet size*

At the injection point $z_{\rm min} = 10^9$ cm, we set the initial cylindrical radius of the jet to be $r_0 = 8 \times 10^7$ cm. The initial cylindrical radius should be smaller than the value in Eq. (26) that will be the cylindrical radius of the jet af-

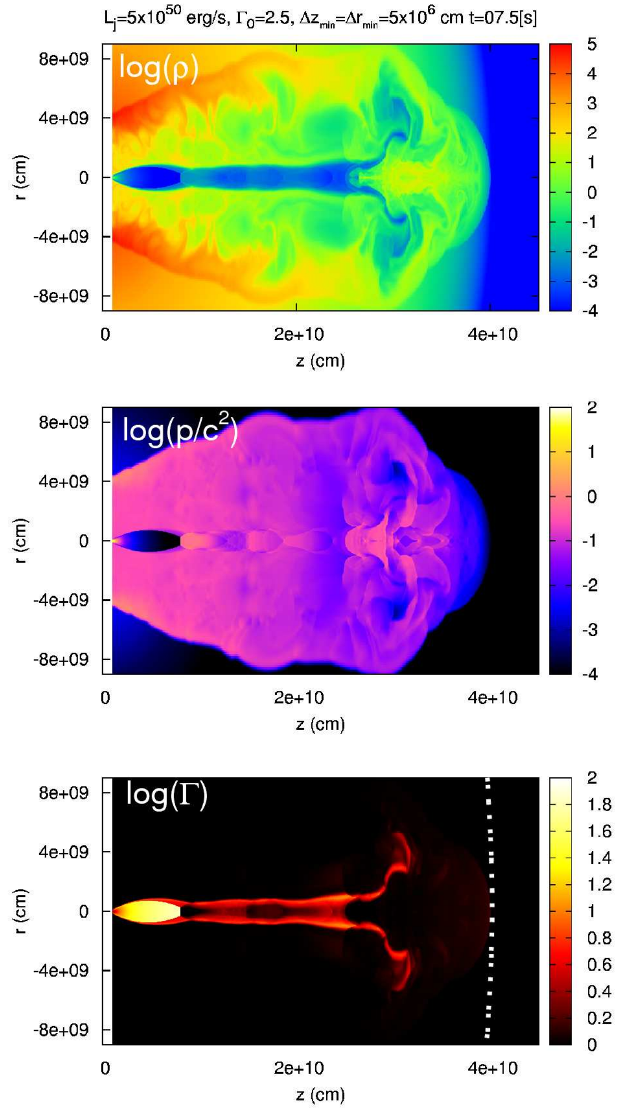

FIG. 13.— Same as Fig. 4 but $\Gamma_0 = 2.5$ with a high resolution (model G2.5H), just before the shock breakout ($t = 7.5$ s).

ter the collimation shock. Otherwise, the jet evolution is different. The jet does not show an initial expansion but keeps the incorrect cylindrical radius. This gives wrong dynamics for such as the breakout time, the cocoon energetics, and the opening angle. That is why we start the numerical simulation with so small initial cylindrical radius. At least several or ten grid points are necessary for covering the initial cylindrical radius because we have to resolve the internal shocks. This requests us to use fine grid points as used in this study. Our simulations use one of the finest resolutions so far.

3.9. *Comparison with previous studies*

We have done one of the most highest resolution calculations for hydrodynamic simulations of the jet propagation. High resolutions reduce the numerical baryon loading which affects the jet dynamics. Since the numerical baryon loading is the most dangerous at the boundary with a high contrast of the enthalpy h, the highest resolution grid points are devoted to the region which covers the jet and some part of the cocoon. The highest resolution grid size is comparable or better than that used in Morsony et al. (2007); Lazzati et al. (2013). The highest resolution region is much larger than that used in Morsony et al. (2007).

Since we have done quite high resolution calculations for hydrodynamic simulations of the jet dynamics, the computational domain is restricted to about ten times larger than the progenitor size. This is smaller than that used in Mizuta et al. (2011); Nagakura et al. (2011); Suzuki & Shigeyama (2013). Our discussion is restricted only for several seconds after the jet breakout. The computational box size is comparable with that used in Morsony et al. (2007) who discussed the time evolution of the opening angle of the jet. The requirement that the initial cylindrical radius of the jet should be sufficiently small is also one of the reasons to use high resolution grid points (see Sec. 3.8). We have paid a special care with this by taking a sufficiently small cylindrical radius of the initial jet. The dynamics of our results may be different from those done by Morsony et al. (2007) who take the initial cylindrical radius to $\sim 2 \times 10^8$ cm for $\theta_0 = 10$ degrees case. This is about three times larger than our initial cylindrical radius of the jet ($r_0 = 8 \times 10^7$ cm).

Our numerical results show that the opening angle of the jet after jet breakout is narrower than that we expect ($\theta_j \sim 1/\Gamma_0$). This trend is consistent with previous numerical simulations, for example, Morsony et al. (2007); Lazzati et al. (2009); Mizuta et al. (2011); Lazzati et al. (2013) who have pointed out that the opening angle after the jet breakout is smaller than the initial opening angle (θ_0). In this paper we introduce much more sophisticated analysis with probe particles which allow us to follow the Lagrange motion of each element. We find out the correlation between the initial Lorentz factor and the opening angle of the jet, i.e., $\theta_j \sim 1/5\Gamma_0$. We also find where and how the gas starts the free expansion. The position to start the free expansion is off-center and also different for each particle around $\sim 4 \times 10^{10}$ cm. We identify that the jet breakout acceleration occurs and the local Lorentz factor of the flow just before the free expansion determines the opening angle of the jet. Since we measure the opening angle by the free expansion direction respect to the jet axis, the angle is different from that measured by Morsony et al. (2007) who defined the jet opening angle by measuring how the GRB jet component ($\Gamma_{\rm inf} \equiv h\Gamma \geq \Gamma_{cr}$) spreads out at $R = 1.2 \times 10^{11}$ cm in the spherical coordinate (the progenitor center is the origin of the coordinate). The different measurement methods result in about 30 percents difference in the opening angle of the jet.

4. ANALYTIC MODEL

Let us consider the analytic models for the jet propagation and the dynamics of the opening angle. The evolution is generally divided into two phases, i.e., before and after the jet breakout.

In Sec. 4.1, we discuss the pre-breakout phase. Bromberg et al. (2011) investigated the pre-breakout evolution in detail. Before the breakout, the jet is inside the progenitor star and collimated by the cocoon pressure. Since the cocoon pressure is constant (subsonic inside), the jet becomes cylindrical through the first collimation shock. The cylindrical (and stationary) flow has a constant Lorentz factor because of the flux conservation. If the Lorentz factor were constant even at the jet breakout, the opening angle of the jet would be an inverse of the initial Lorentz factor (or the initial opening angle; see below) as shown in Fig. 1, but this is not the case as shown in the next Sec. 4.2.

We present analytical formulae of the jet propagation for easy comparison with our numerical simulations, and make a calibration of the model parameter taking great care of the baryon contamination and the initial jet size. We compare the evolution of three physical quantities, the jet head position, the jet cylindrical radius, and the collimation position, with numerical calculations. The model has one free parameter η in Eq. (8), which is obtained by a fitting to the numerical results.

In Sec. 4.2, we argue the post-breakout phase. After the breakout, the cocoon pressure is not constant but decreasing outward (see Fig. 5). This leads to less collimation, wider jet, and hence larger Lorentz factor. Therefore, the jet-breakout acceleration occurs almost inevitably if the external medium has a finite size. We estimate that the jet-breakout acceleration boosts the Lorentz factor of the jet by a factor of several ~ 5. This is the reason why the naive picture in Fig. 1 is not correct but the jet opening angle becomes $\sim 1/5\Gamma$ as shown numerically in Sec. 3.4 and Fig. 8.

4.1. *Jet evolution in constant external pressure*

First we consider the jet evolution inside the progenitor star. Bromberg et al. (2011) give detail analyses. Here we make the analytical formulae easier to use in the calibration of the model parameters. The jet dynamics is controlled by three processes, (1) jet head, (2) cocoon, and (3) collimation. After combining these dynamics, we can give the evolution of the jet head position in Eq. (25), the jet cylindrical radius in Eq. (26), and the collimation position in Eq. (27). There is one free parameter η in Eq. (8) to be fixed by numerical simulations.

(1) *Jet head dynamics*: After propagating inside the star, the jet collides with the stellar envelope. A reverse shock decelerates the jet, and a forward shock runs into the stellar envelope. The shocked region is called the jet head. The jet head dynamics is determined by the ram pressure balance between the shocked jet and the shocked envelope, both of which are given by the pre-shock quantities through the shock jump conditions (Marti et al. 1997; Mészáros & Waxman 2001; Matzner 2003),

$$h_j \rho_j c^2 \Gamma_{jh}^2 \beta_{jh}^2 + P_j = h_a \rho_a c^2 \Gamma_h^2 \beta_h^2 + P_a, \tag{4}$$

where $\Gamma_{jh} = \Gamma_j \Gamma_h (1 - \beta_j \beta_h)$ is the relative Lorentz factor between the jet and the jet head, and $\beta_{jh} = (\beta_j - \beta_h)/(1 - \beta_j \beta_h)$ is the corresponding relative velocity. We can neglect the internal pressure of the jet P_j for the strong reverse shock and the pressure P_a for the cold ambient matter. Then the jet head velocity is obtained as

$$\beta_h = \frac{\beta_j}{1 + \tilde{L}^{-1/2}}, \tag{5}$$

where

$$\tilde{L} \equiv \frac{h_j \rho_j \Gamma_j^2}{h_a \rho_a} \simeq \frac{L_j}{\Sigma_j \rho_a c^3}, \tag{6}$$

is the ratio of the energy density between the jet and the ambient medium. In the last equality, we assume the cold ambient medium $h_a = 1$, and use the jet cross-section $\Sigma_j = \pi r_j^2$ and the jet luminosity L_j. For typical parameters of GRBs, we have $\tilde{L} \ll 1$, i.e., a non-relativistic head velocity,

$$\beta_h \simeq \tilde{L}^{1/2}. \tag{7}$$

Hereafter we consider the non-relativistic case.

(2) *Cocoon*: The shocked jet and the shocked envelope try to expand and go sideways into a cocoon component. The cocoon pressure is determined by the injected energy divided by the cocoon volume (Begelman & Cioffi 1989),

$$P_c = \frac{E}{3V_c} = \frac{\eta}{3} \frac{\int L_j (1 - \beta_h) dt}{(\int \beta_h c\, dt)\, \pi (\int \beta_c c\, dt)^2}, \tag{8}$$

where η is $O(1)$ parameter to correct the approximation of the cylindrical cocoon shape. We will use η to absorb other approximations, such as that we represent the transverse velocity by a single value, and determine η by comparing the analytic formulae with the numerical simulations. Note $1 - \beta_h \approx 1$ for the non-relativistic head velocity. The transverse velocity of the cocoon is determined by the balance between the cocoon pressure and the ram pressure of the ambient medium,

$$\beta_c = \sqrt{\frac{P_c}{\bar{\rho}_a c^2}}, \tag{9}$$

where

$$\bar{\rho}_a(z_h) = \frac{\int \rho_a dV}{V_c} \equiv \xi_a \rho_a(z_h), \tag{10}$$

is the mean density of the medium. Defining

$$\int \beta_h\, dt \equiv \xi_h \beta_h t \left(= \frac{z_h}{c} \right), \quad \int \beta_c\, dt \equiv \xi_c \beta_c t, \tag{11}$$

we can eliminate β_c from Eqs. (8) and (9) to obtain

$$P_c = \tilde{L}^{-1/4} \left(\frac{L_j \rho_a}{c t^2} \right)^{1/2} \left(\frac{\eta \xi_a}{3\pi \xi_h \xi_c^2} \right)^{1/2}. \tag{12}$$

If the density profile follows a power-law $\rho_a \propto z^{-\alpha}$, the coefficients, ξ_a, ξ_h and ξ_c, become constant,

$$\xi_a = \frac{3}{3 - \alpha}, \quad \xi_h = \xi_c = \frac{5 - \alpha}{3}. \tag{13}$$

Here we obtain ξ_a in Eq. (10) assuming a spherical cocoon with a radius z_h for simplicity. Although this is not a good approximation, we adjust η in Eq. (8) to fit the analytic models with numerical results. For ξ_h and ξ_c, we use Eqs. (22), (9) and (23), which yield $\beta_h \propto t^{-2/5} (\beta_h t)^{\alpha/5} \propto t^{\frac{\alpha-2}{5-\alpha}}$ and $\beta_c \propto t^{-2/5} (\beta_h t)^{\alpha/5} \propto t^{\frac{\alpha-2}{5-\alpha}}$.

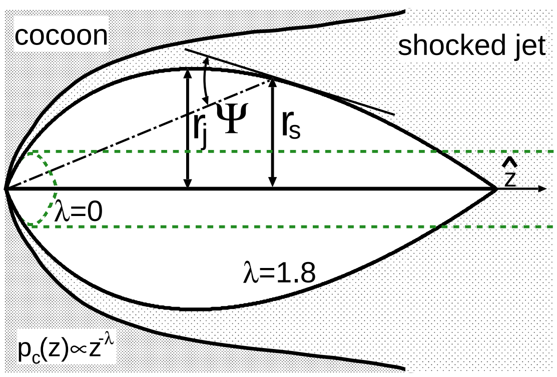

FIG. 14.— Structure of the jet and the collimation shock. The collimation shock appears by the interaction between the expanding jet and the high pressure cocoon. The collimation shock converges at $\hat{z}$. Solid lines show the collimation shock and the jet structure after the collimation shock for a decreasing pressure case ($\lambda = 1.8$), whereas green colored dashed lines show the collimation shock and the cylindrical jet structure after the collimation shock for a constant pressure case ($\lambda = 0$).

(3) *Collimation shock*: If the ambient density is sufficiently high like in the stellar envelope, the cocoon pressure becomes high enough to collimate the jet. The initially expanding jet hits the first collimation shock and converges its trajectory. For a constant cocoon pressure, the conical jet becomes cylindrical after the collimation. This process determines the cross-section of the jet and thereby the jet Lorentz factor after the shock.

The geometry of the collimation shock is determined by the pressure balance between the jet and the cocoon (Komissarov & Falle 1997; Bromberg et al. 2011),

$$h_0\rho_0 c^2\Gamma_0^2\beta_0^2\sin^2\Psi + P_0 = P_c, \tag{14}$$

where the first term is the ram pressure of the jet normal to the shock surface (see Fig. 14), the subscript 0 stands for the unshocked jet. Since the jet internal pressure decreases $P_0 \propto z^{-4}$ as the size grows, we neglect the term P_0. For a small incident angle, we have a relation

$$\sin\Psi = \frac{r_s}{z} - \frac{dr_s}{dz} = z\frac{d}{dz}\left(\frac{r_s}{z}\right), \tag{15}$$

to a first order (see Fig. 14), where r_s is the cylindrical radius of the shock position. Then equation (14) gives a first-order ordinary differential equation. Noting $\beta_0 \approx 1$ and $L_j \simeq h_0\rho_0 c^3\Gamma_0^2(\pi z^2\theta_0^2)$, we can integrate the geometry of the collimation shock as

$$r_s = \theta_0 z(1 + Az_*) - \theta_0 A z^2, \tag{16}$$

where A is given by Eq. (17). We note that we assume a constant external pressure P_c =const. For a decreasing external pressure, the shock geometry is different as shown in the next Sec. 4.2.

According to Eq. (16), the collimation shock expands to a maximum size at $\frac{dr_s}{dz}|_{z=z_{\max}} = 0$, and converges to $r_s(z = \hat{z}) = 0$ where the maximally-expanding position $z_{\max}$ and the converging position $\hat{z}$ are given by

$$\hat{z} = 2z_{\max} = A^{-1} + z_* \simeq A^{-1} = \sqrt{\frac{L_j\beta_0}{\pi c P_c}}. \tag{17}$$

In the second last equality we assume that the collimation shock is initially small $z_* \ll A^{-1}$. As we can see from Fig. 14, the maximum size of the collimation shock determines the cross-section of the jet after the collimation shock,

$$\Sigma_j(z > \hat{z}) \simeq \pi\left(\theta_0 z_{\max}\right)^2 \simeq \frac{L_j\theta_0^2}{4cP_c}. \tag{18}$$

Combining with a general relation for a hot jet (radiation-dominated jet),

$$L_j \simeq 4P_c\Gamma_1^2\Sigma_j c, \tag{19}$$

we obtain the Lorentz factor of the jet after the first collimation shock (Bromberg et al. 2011),

$$\Gamma_1 \simeq \frac{1}{\theta_0}. \tag{20}$$

After the collimation shock, the jet is usually over-deflected to the axis, resulting in an oblique shock inside the jet. A high pressure region appears after the converging point of the first collimation shock and then expands again. The jet repeats a cycle of a bounce, expansion and collimation, like a spring under the pressure of the cocoon. Because the supersonic jet is not synchronized with the cocoon, the oblique shocks arise in the jet. In each collimation, the jet tries to expand with the same angle $\sim 1/\Gamma_0$ and hence the Lorentz factor after a collimating oblique shock keeps the same value. The Lorentz factor after the N-th collimating oblique shock is

$$\Gamma_N \simeq \Gamma_{(N-1)} \simeq \ldots \simeq \Gamma_1 \simeq \frac{1}{\theta_0} \simeq \Gamma_0, \tag{21}$$

under a constant pressure inside a star. The last equality is satisfied in our simulation because we inject a jet parallel to the z-axis and the jet tries to expand with an angle $\theta_0 \sim 1/\Gamma_0$ about an inverse of the initial Lorentz factor.

If the Lorentz factor were constant $\Gamma \sim \Gamma_0$ even at the jet breakout, the opening angle of the jet would be the inverse of the Lorentz factor inside a star (or the initial opening angle) $\theta_j \sim \Gamma_0^{-1} \sim \theta_0$. However this is not the case as discussed in the next subsection 4.2.

For comparison with the numerical results, we express physical quantities by basic parameters, i.e., the jet luminosity L_j, the ambient density ρ_a, the initial opening angle θ_0, and time t. First, we rewrite the head velocity and the cocoon pressure as

$$\beta_h \simeq \tilde{L}^{1/2} \simeq \left(\frac{L_j}{c^5 t^2\rho_a\theta_0^4}\right)^{1/5}\left(\frac{16}{3\pi}\frac{\eta\xi_a}{\xi_h\xi_c^2}\right)^{1/5}, \tag{22}$$

$$P_c = \left(\frac{\rho_a^3 L_j^2\theta_0^2}{t^4}\right)^{1/5}\left(\frac{1}{6\pi}\frac{\eta\xi_a}{\xi_h\xi_c^2}\right)^{2/5}, \tag{23}$$

respectively, with equations (6), (7), (12) and (18). Then we can derive analytic formulae for the jet head position with Eqs. (11) and (22), the jet cylindrical radius with Eqs. (18) and (12), and the converging point of the collimation shock with Eqs. (17) and (12) as

$$z_h = \xi_h\beta_h ct \simeq \left(\frac{t^3 L_j}{\rho_a\theta_0^4}\right)^{1/5}\left(\frac{16}{3\pi}\frac{\eta\xi_a\xi_h^4}{\xi_c^2}\right)^{1/5} \tag{24}$$

$$\simeq 1.4\times 10^{10}\,\mathrm{cm}\left(\frac{t}{1\,\mathrm{s}}\right)^{3/5}\left(\frac{L_j}{10^{52}\,\mathrm{erg\,s^{-1}}}\right)^{1/5}$$

$$\times\left(\frac{\rho_a}{10^4\,\mathrm{g\,cm^{-3}}}\right)^{-1/5}\left(\frac{\theta_0}{0.1}\right)^{-4/5}, \tag{25}$$

$$\begin{aligned} r_j \equiv \left(\frac{\Sigma_j}{\pi}\right)^{1/2} &\simeq \left(\frac{t^4 L_j^3 \theta_0^8}{c^5 \rho_a^3}\right)^{1/10}\left(\frac{3}{16\pi^{3/2}}\frac{\xi_h \xi_c^2}{\eta \xi_a}\right)^{1/5} \\ &\simeq 2.4\times 10^8\,\mathrm{cm}\left(\frac{t}{1\,\mathrm{s}}\right)^{2/5}\left(\frac{L_j}{10^{52}\,\mathrm{erg\,s^{-1}}}\right)^{3/10} \\ &\times\left(\frac{\rho_a}{10^4\,\mathrm{g\,cm^{-3}}}\right)^{-3/10}\left(\frac{\theta_0}{0.1}\right)^{4/5}, \end{aligned} \tag{26}$$

$$\begin{aligned} \hat{z} &\simeq \left(\frac{t^4 L_j^3}{c^5 \rho_a^3 \theta_0^2}\right)^{1/10}\left(\frac{6}{\pi^{3/2}}\frac{\xi_h \xi_c^2}{\eta \xi_a}\right)^{1/5} \\ &\simeq 4.7\times 10^9\,\mathrm{cm}\left(\frac{t}{1\,\mathrm{s}}\right)^{2/5}\left(\frac{L_j}{10^{52}\,\mathrm{erg\,s^{-1}}}\right)^{3/10} \\ &\times\left(\frac{\rho_a}{10^4\,\mathrm{g\,cm^{-3}}}\right)^{-3/10}\left(\frac{\theta_0}{0.1}\right)^{-1/5}, \end{aligned} \tag{27}$$

respectively, where we set $\alpha = 2$ [$\xi_a = 3$, $\xi_h = \xi_c = 1$ in Eq. (13)] and $\eta = 0.01$ for the numerical values. For a general density profile rather than a power-law form, we solve the first-line equation (24) for the head position z_h, where the quantities ρ_a, ξ_a, ξ_h and ξ_c in the right-hand-side are also functions of z_h. Here, for simplicity, we set ξ_a, ξ_h and ξ_c with Eq. (13) by using the density slope $\alpha = -d\ln\rho_a/d\ln z$ at $z = z_h$.

As shown in Sec. 3, we can fit three analytic formulae in Eqs. (25), (26) and (27) with the numerical calculations by adjusting one parameter $\eta \sim 0.01$ in Eq. (8). Figure 15 shows the comparison with analytic formulae and the results of the hydrodynamic simulations, i.e., the head position, the converging position, and the jet radius, for the model G5.0 ($\Gamma_0 = 5$ and $\Delta z_{\min} = \Delta r_{\min} = 10^7$cm). The numerical results provide good agreement with the analytic ones. The difference in the early evolution of the jet is caused by the insufficient smallness of the initial jet size. Since the power law index (α) in the mass density profile exceeds $\alpha > 3$ at a certain radius and ξ_a becomes infinity or negative in Eq. (13), we can not apply the analytic formula after $t = 1.05$ s. Figure 15 is the confirmation that the analytic physical picture by Bromberg et al. (2011) is correct[3] by the numerical calculations that take great care of the baryon loading and the initial jet size.

4.2. *Jet evolution in decreasing external pressure*

We numerically find that the opening angle of the jet is not $\sim 1/\Gamma_0$ but $\sim 1/5\Gamma_0$ where Γ_0 is the Lorentz factor of the jet inside a star. This is because the cocoon expands to the outer space and hence the cocoon pressure decreases outward after the jet breakout from the stellar surface. In the decreasing pressure, the jet becomes less collimated and hence more accelerated than that in the star. Since the jet-breakout acceleration increases the Lorentz factor Γ before a free expansion, the jet opening angle determined by $\sim 1/\Gamma$ is narrower than the naive estimate.

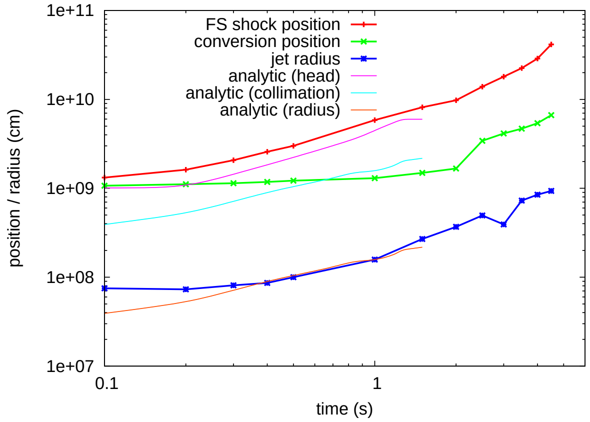

FIG. 15.— Comparison of the numerical results with the analytical formulae for the jet propagation inside the star (see Sec. 4.1). We show the forward shock position of the jet head z_h, the converging position of the collimation shock $\hat{z}$, and the maximum cylindrical radius of the jet $r_{s,\max} \simeq \theta_0 z_{\max}$. Theoretical model lines are also plotted. Since the slope of the radial mass density profile starts to rapidly drop at $R \sim 6\times 10^9$ cm, there is no analytic solution outside this point.

The jet-breakout acceleration is broadly divided into two types, i.e., with and without a shock. The both types contribute equally to the Lorentz factor enhancement.

First we consider the jet-breakout acceleration by evaluating the Lorentz factor after the collimating oblique shock. The cocoon pressure that is decreasing outward is expressed by

$$P_c(z) = P_*\left(\frac{z}{z_*}\right)^{-\lambda}. \tag{28}$$

Under this pressure, we can solve the geometry of the collimation shock, as in the previous section 4.1 with Eqs. (14) and (15),

$$r_s = \theta_0 z\left(1 + \frac{A_* z_*}{1-\frac{\lambda}{2}}\right) - \frac{\theta_0 A_* z^2}{1-\frac{\lambda}{2}}\left(\frac{z}{z_*}\right)^{-\frac{\lambda}{2}}, \tag{29}$$

where z_* is the initial position of the collimation shock and

$$A_* = \sqrt{\frac{\pi c P_*}{L_j \beta_0}}. \tag{30}$$

We show the shock geometry in Fig. 14. Note that the shock geometry is not parabola but sleek in contrast to the constant pressure case in Eq. (16). The collimation shock expands to a maximum cylindrical radius at $\frac{dr_s}{dz}|_{z=z_{\max}} = 0$, where the maximally-expanding position is given by

$$\frac{z_{\max}}{z_*} = \left[\left(\frac{2-\lambda}{A_* z_*} + 2\right)\frac{1}{4-\lambda}\right]^{\frac{2}{2-\lambda}}. \tag{31}$$

Here $\lambda < 2$ is necessary for the shock to converge. At the position $z_{\max}$, the general relation for a hot jet in Eq. (19) is given by

$$L_j \simeq 4\left[P_*\left(\frac{z_{\max}}{z_*}\right)^{-\lambda}\right]\Gamma_1^2\left(\pi\theta_0^2 z_{\max}^2\right)c. \tag{32}$$

---

[3] Although $\eta \sim 0.01$ is smaller than $O(1)$, a factor ~ 2 difference in z_h in Eq. (24) may cause a factor $2^5 \sim 32$ difference in η.

This yields the Lorentz factor after the collimation shock,

$$\Gamma_1 \simeq \frac{1}{\theta_0} \times \mathcal{A}, \tag{33}$$

which is larger than that for a constant pressure case in Eq. (20) by

$$\mathcal{A} = \frac{4-\lambda}{4-2\lambda+4A_* z_*} \simeq \frac{4-\lambda}{4-2\lambda} \sim 5, \quad \text{if} \quad \lambda \sim 1.8, \tag{34}$$

for small $A_* z_*$. To be precise, θ_0 is not the initial opening angle of the jet here, but the opening angle of the jet expanding to the last collimating oblique shock, which is the inverse of the Lorentz factor inside a jet $\sim \Gamma_0^{-1}$ and thereby turns out to be θ_0 from Eqs. (20) and (21).

The numerical calculations show that the total acceleration factor is $\mathcal{A} \sim 5$ (see Fig. 15), about half of which is achieved at the collimation shock and the other half of which is obtained later. A factor ~ 2.5 can be explained by $\lambda \sim 1.5$. Although it is difficult to estimate the exact acceleration factor $\mathcal{A}$ analytically, we can see that $\mathcal{A}$ is mainly determined by the slope λ of the external pressure profile. In our case, the external pressure profile is shaped by the cocoon expansion to the outer space, which does not depend on the jet properties so much. Therefore it is natural that similar acceleration factors are obtained for different initial conditions in our numerical calculations.

Next we consider a jet-breakout acceleration without shocks (i.e., an adiabatic jet) as the other extreme. The jet expands in a decreasing pressure, lowering its temperature as radiation $T' \propto V'^{-1/3}$ where V' is the comoving volume of the jet. If the pressure balances between the jet and the cocoon $T'^4 \propto P_c$, the jet does not perform work and hence the energy is conserved $\Gamma T'^4 V' \sim$ const. Therefore the jet accelerates as the size grows according to (Ioka et al. 2011)

$$\Gamma \propto T'^{-1} \propto P_c^{-1/4} \propto z^{\lambda/4}. \tag{35}$$

In the numerical calculations, we identify such an adiabatic evolution after the collimation shock, in particular at the periphery of the jet. For $2 < \lambda < 4$, the cocoon pressure does not causally affect the jet interior (Ioka et al. 2011) but still affect the periphery of the jet. Note that the off-center origin makes the pressure profile shallower than that shown in Fig. 5 with the stellar center origin.

In order to estimate the acceleration factor of the Lorentz factor, we need to know how much the jet expands before entering a free expansion phase. In this regard, we should note that the jet expands from the breakout position, that is, the fireball of the jet is off-centered by the cocoon confinement. This means that the fireball size should not be measured from the center of the star. Instead, the effective center of the fireball locates at a distance $\sim \Gamma_0 r_j \sim r_j/\theta_0$ inward from the stellar surface (breakout point) because the jet tries to expand with an opening angle of $1/\Gamma_0$ and the expanding surface has an initial cylindrical radius of r_j in Eq. (26). So the initial fireball size is

$$r_0 \sim \Gamma_0 r_j \sim r_j/\theta_0. \tag{36}$$

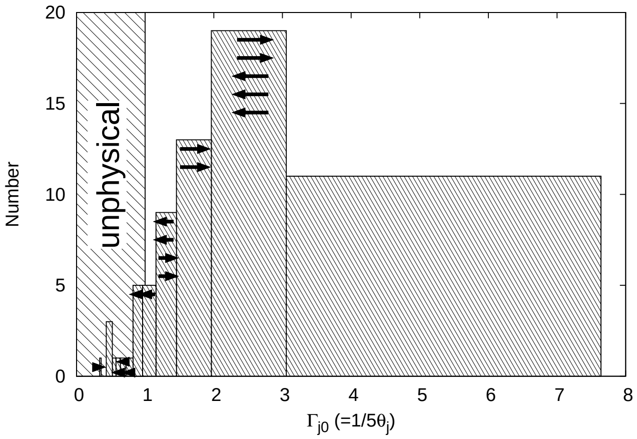

Fig. 16.— Distribution of the initial Lorentz factor of the jet inferred by the observations and the relation $\Gamma_0 = 1/5\theta_j$ in Eq. (3). Observational data (θ_j, N) are taken from Fig. 6 in Fong et al. (2012). Since a Lorentz factor should be greater than unity, the region with $\Gamma_0 < 1$ is shaded as an unphysical zone.

If the fireball expands to a size of the stellar radius $R \sim 4 \times 10^{10}$ cm, the expansion factor is about ~ 10 times for typical parameters in Eq. (26) and hence the Lorentz factor grows by a factor ~ 3 for $\lambda \sim 2$ according to Eq. (35). Thus the adiabatic expansion can explain a part of the jet-breakout acceleration observed in the numerical calculations. Here a parameter dependence of the expansion factor is weak since the initial fireball size is $r_0 \propto L_j^{1/6} \rho_a^{-1/6} \theta_0^{1/3}$ at the breakout time (when $R \sim z_h$) with Eqs. (25) and (26). Note that the jet-breakout acceleration looks very rapid at the first glance if we do not notice the off-center effect (i.e., the radius measured from the stellar center is only doubled).

5. DISCUSSIONS

5.1. *Lorentz factor of the jet in a star*

The opening angle of the GRB jet is usually measured by observing a jet break in the afterglow lightcurve (Racusin et al. 2009, 2011; Fong et al. 2012). Our numerical and analytic calculations show that a jet opening angle is related with the Lorentz factor inside a star as

$$\theta_j \sim \frac{1}{5\Gamma_0}. \tag{37}$$

By applying this formula, we can infer the Lorentz factor inside a star (or the initial opening angle) from the observed opening angle of the GRB jet. Figure 16 shows the estimated Lorentz factor inside a star. The result suggests that the jet is mildly relativistic in a star (or the initial opening angle is O(0.3-0.5) radian).

The slow jet inside a star is a preferable condition for the survival of nuclei in the jet, which may explain the observed ultra-high energy cosmic-ray nuclei (Murase et al. 2008; Wang et al. 2008; Metzger et al. 2011; Horiuchi et al. 2012).

Equation (37) also implies that the maximum opening angle is obtained by setting $\Gamma_0 \sim 1$ as

$$\theta_{j,\max} \sim 1/5 = 0.2 \sim 12^\circ, \tag{38}$$

if the jet is radiation-dominated at the breakout. However several events violate this maximum as shown in

Fig. 16 (Racusin et al. 2009, 2011; Fong et al. 2012). A possible solution to this problem is to consider a baryon-rich slow sheath surrounding a central jet. A baryon-rich flow cannot accelerate to a large Lorentz factor, and if the Lorentz factor of the baryon-rich sheath is less than ~ 5, the opening angle of the sheath can be larger than ~ 0.2. Note that the central jet should have $\Gamma > 100$ to avoid the compactness problem.

5.2. *Amati and Yonetoku relations*

Based on our numerical and analytical analyses, we can evaluate the initial condition of a jet that is just expanding freely, and infer the observational characteristics of the jet based on the photosphere model (e.g., Pe'er et al. 2007; Ioka et al. 2007). First, since we are now able to estimate the opening angle of the jet in Eq. (37), we can assess the isotropic luminosity of the jet,

$$L_{\rm iso} = \frac{L_j}{\pi\theta_j^2} \propto L_j \Gamma_0^2. \tag{39}$$

We can also obtain the observed temperature of a jet if it is radiation-dominated,

$$E_{\rm peak} \sim T_{\rm obs} \propto \Gamma_0 T' \propto \Gamma_0 P_c^{1/4}, \tag{40}$$

which may be identified with the spectral peak energy $E_{\rm peak}$ of a GRB in the photosphere model. In the actual observations of GRBs, there is a relation between the isotropic luminosity and the observed temperature,

$$E_{\rm peak} \propto L_{\rm iso}^{1/2} \quad \text{(Yonetoku relation)}, \tag{41}$$

so-called the Yonetoku relation (Yonetoku et al. 2004).

Let us show that the Yonetoku relation is reproduced if the total jet luminosity is nearly proportional to the Lorentz factor inside a star

$$L_j \propto \Gamma_0, \tag{42}$$

that is, the mass outflow rate is $\dot{M} = L_j/\Gamma_0 \sim$ const. First, the above equation gives $L_{\rm iso} \propto \Gamma_0^3$ with Eq. (39). Next, substituting Eqs. (39) and (40) into Eq. (19) (where we should read Γ_1 as Γ_0) yields

$$E_{\rm peak} \propto L_{\rm iso}^{1/4} \Sigma_j^{-1/4}. \tag{43}$$

Here the jet cross-section follows $\Sigma_j \propto L_j^{1/3}\theta_0^{8/3}$ at the time

$$t \propto L_j^{-1/3}\theta_0^{4/3}, \tag{44}$$

of the jet breakout, $z_h \sim R_*$ (when the jet head reaches the stellar surface) with Eqs. (25) and (26).[4] Then, noting $\theta_0 \sim \Gamma_0^{-1}$, we have

$$E_{\rm peak} \propto L_{\rm iso}^{1/4}\Gamma_0^{7/12} \propto L_{\rm iso}^{4/9}, \tag{45}$$

which is close to the Yonetoku relation.

In addition, we may be also able to reproduce the Amati relation (Amati et al. 2002),

$$E_{\rm peak} \propto E_{\rm iso}^{1/2} \quad \text{(Amati relation)}. \tag{46}$$

We can think that the GRB duration is roughly given by the sound-crossing time across the cocoon of the stellar size,

$$T_{90} \sim \frac{R_*}{c\beta_c} \propto t^{2/5} L_j^{-1/5}\theta_0^{-1/5} \propto L_j^{-1/3}\theta_0^{1/3} \propto L_{\rm iso}^{-2/9}, \tag{47}$$

with Eq. (9) and (23), because the cocoon pressure decreases after this time, leading to less confinement, larger opening angle, and smaller isotropic luminosity of the jet. Note that the weak correlation between T_{90} and $L_{\rm iso}$ is actually observed. Then we can estimate the isotropic energy

$$E_{\rm peak} \propto L_{\rm iso}^{4/9} \propto (L_{\rm iso}T_{90})^{4/7} \sim E_{\rm iso}^{4/7}, \tag{48}$$

which is also similar to the Amati relation. This is killing two birds with one stone, that is, we explain two relations (Amati and Yonetoku relations) by only one assumption in Eq. (42).

6. SUMMARY

In this paper we have explored the dynamics of the GRB jets from collapsars by performing 2D relativistic hydrodynamic simulations as well as the analytical analyses. We have followed the jet propagation all the way from the progenitor star through the jet breakout to the free expansion, with implementing probe particles to trace the Lagrange motion of the fluid elements. This enable us to connect the final jet appearance to the initial jet condition near the central engine.

We have found that the jet opening angle after the jet breakout is about $\theta_j \sim 1/5\Gamma_0$ in Eq. (3) and Fig. 9 where Γ_0 is the initial Lorentz factor of the jet injected into the progenitor star. This value is smaller than the naive expectation $\theta_j \sim 1/\Gamma_0$ in Fig. 1, where we thought that the opening angle is determined by the inverse of the Lorentz factor and the Lorentz factor keeps the initial value Γ_0 for a cylindrical jet. Actually this is partly correct. The jet becomes cylindrical under the nearly homogeneous pressure of the cocoon after crossing the first collimation shock. The Lorentz factor after the collimation shock is $\sim \Gamma_0$ and largely stays constant before the jet breakout according to our simulations. However we have identified the "jet-breakout acceleration" (just before and) after the jet breakout. This occurs because the pressure profile of the cocoon can not keep constant but decreases outward as the cocoon expands to the outer space. The cocoon still confines the jet to some extent near the stellar radius, while the jet expands its cylindrical radius with increasing its Lorentz factor by a factor ~ 5 before a free expansion. Therefore the jet opening angle becomes narrow, which is determined by the inverse of the Lorentz factor at the base of the free expansion, as explicitly shown by the numerical simulations. The opening angles are roughly constant over time with a factor ~ 2 fluctuations in Fig. 8.

We have also analytically analyzed the jet-breakout acceleration. The jet-breakout acceleration occurs with and without the collimating oblique shock, and both are equally important. For the former case, we solve the structure of the collimating oblique shock in a decreasing pressure profile and obtain the Lorentz factor after the shock in Eq. (33). The post-shock Lorentz factor is enhanced appreciably for a pressure slope close to $\lambda \sim 2$

---

[4] We assume that the structure of the progenitor star is similar and neglect the dependence on it.

in $P \propto z^{-\lambda}$. The latter case happens after the last collimating oblique shock, even for $\lambda > 2$ near the periphery of the jet in Eq. (35).

We have also compared our numerical results with the analytical formulae for a jet propagation inside the star presented by Bromberg et al. (2011), and have confirmed good agreements. For later use, we have calibrated the model parameter with the numerical results. We can now calculate the jet evolution relatively precisely with ease, such as the jet head position, the jet cylindrical radius, and the converging position of the collimation shock, for a wide range of initial conditions.

We have paid special attention to the numerical diffusion of the baryon loading into the jet through the discontinuity, which can entirely change the jet propagation. We have also taken the initial cylindrical radius of the jet sufficiently smaller than the to-be radius after the first collimation shock because a large initial radius slows down the jet propagation. For these purposes, we have performed one of the highest resolution calculations so far.

The post-breakout jet shows a hollow-cone angular structure. The edge is relatively sharp with an exponential drop. The bright rim is produced by the shock between the expanding jet and the high pressure cocoon before the free expansion.

To understand the jet evolution, it is important to notice that the jet makes an off-center expansion as a result of the cocoon confinement. If the expansion origin is the stellar center, the fireball would feel a steep pressure profile of the cocoon pressure and the acceleration would be slow. In addition, the opening angle should be measured from the off-center origin for precise analyses.

We have also applied our results to the observations. First we infer the initial Lorentz factor Γ_0 of the jet injected at the central engine by using the observed opening angles in Fig. 16. The distribution of Γ_0 peaks at around $\sim$ 2–3. Second our result suggests the existence of a maximum opening angle for a high-entropy jet, $\theta_{j,\max} \sim 1/5 \sim 12^\circ$, in Eq. (38). However several bursts violate this maximum value. This may imply a two-component jet with a baryon-rich slow sheath surrounding a central jet.

We have also derived Amati and Yonetoku spectral relations by applying our results to the photosphere of the jet that is expanding freely after the jet breakout. We explain both the relations with only one assumption of a constant rate of the mass outflow $\dot{M} = L_j/\Gamma_0 \sim$ const from the central engine in Eq. (42). The fireball temperature becomes different from the value at the central engine after the jet propagation through the star. Thus the confinement by the cocoon and the off-center expansion of the jet may be the missing pieces for the photosphere model so far.

In the future, it is interesting to study the long-term evolution of the jet studied in this paper and the evolution of the low-luminosity jet and the two-component jet. It is also important to investigate the jet propagation in a huge progenitor such as the Population III GRB (Suwa & Ioka 2011; Nagakura, Suwa & Ioka 2012) and the ultra-long GRB (Levan et al. 2013).

We would like to thank A. Heger for his kindness to allow us to use his progenitor models. This work is supported by Grant-in-Aid for Scientific Research from the Ministry of Education, Culture, Sports, Science and Technology (MEXT) of Japan (20105005 (AM), 24103006, 24000004, 22244030, 21684014 (KI)).

REFERENCES

Abdo, A. A., et al., 2009, Science, 323, 1688
Ackermann, M., et al., 2010, Astrophys. J., 716, 1178
Aloy, M. A., Müller, E., Ibáñez, J. M., Martí, J. M., & MacFadyen, A. 2000, ApJ, 531, L119
Amati, L., et al. 2002, A&A, 390, 81
Begelman, M. C., & Cioffi, D. F. 1989, ApJ, 345, L21
Bromberg, O., & Levinson, A. 2009, ApJ, 699, 1274
Bromberg, O., Nakar, E., Piran, T., & Sari, R. 2011, ApJ, 740, 100
Campana, S., et al. 2006, Nature, 442, 1008
Donat, R., & Marquina, A. 1996, Journal of Computational Physics, 125, 42
Fong, W., Berger, E., Margutti, R., et al. 2012, ApJ, 756, 189
Galama, T. J., et al. 1998, Nature, 395, 670
Horiuchi, S., Murase, K., Ioka, K., & Mészáros, P. 2012, ApJ, 753, 69
Ioka, K., Murase, K., Toma, K., Nagataki, S., & Nakamura, T. 2007, ApJ, 670, L77
Ioka, K. 2010, Prog. Theor. Phys., 124, 667
Ioka, K, Ohira, Y., Kawanaka, N., & Mizuta, A. 2011, Prog. Theo. Phys., 126, 555
Iwamoto, K., et al. 1998, Nature, 395, 672
Komissarov, S. S., & Falle, S. A. E. G. 1997, MNRAS, 288, 833
Komissarov, S. S., & Falle, S. A. E. G. 1998, MNRAS, 297, 1087
Lazzati, D., Morsony, B. J., & Begelman, M. C. 2009, ApJ, 700, L47
Lazzati, D., Morsony, B. J., Margutti, R., & Begelman, M. C. 2013, ApJ, 765, 103
Levan, A. J., et al. 2013, arXiv:1302.2352
MacFadyen, A. I., & Woosley, S. E. 1999, ApJ, 524, 262
Marti, J. M. A., Mueller, E., Font, J. A., Ibanez, J. M. A., & Marquina, A. 1997, ApJ, 479, 151
Matzner, C. D. 2003, MNRAS, 345, 575
Mazzali, P. A., et al. 2006, Nature, 442, 1018
Mészáros, P., & Waxman, E. 2001, Physical Review Letters, 87, 171102
Metzger, B. D., Giannios, D., & Horiuchi, S. 2011, MNRAS, 415, 2495
Mizuta, A., Yamada, S., & Takabe, H., 2004, ApJ, 606, 804
Mizuta, A., Yamasaki, T., Nagataki, S., & Mineshige, S. 2006, ApJ, 651, 960
Mizuta, A., & Aloy, M. A. 2009, ApJ, 699, 1261
Mizuta, A., Kino, M., & Nagakura, H. 2010, ApJ, 709, L83
Mizuta, A., Nagataki, S., & Aoi, J. 2011, ApJ, 732, 26
Morsony, B. J., Lazzati, D., & Begelman, M. C. 2007, ApJ, 665, 569
Murase, K., Ioka, K., Nagataki, S., & Nakamura, T. 2008, Phys. Rev. D, 78, 023005
Nagakura, H., Ito, H., Kiuchi, K., & Yamada, S. 2011, ApJ, 731, 80
Nagakura, H., Suwa, Y., & Ioka, K. 2012, ApJ, 754, 85
Pe'er, A., Ryde, F., Wijers, R. A. M. J., Mészáros, P., & Rees, M. J. 2007, ApJ, 664, L1
Racusin, J. L., Liang, E. W., Burrows, D. N., et al. 2009, ApJ, 698, 43
Racusin, J. L., Oates, S. R., Schady, P., et al. 2011, ApJ, 738, 138
Sari, R., Piran, T., & Halpern, J. P. 1999, ApJ, 519, L17
Shu, C.-W., & Osher, S. 1988, Journal of Computational Physics, 77, 439
Stanek, K. Z., et al. 2003, ApJ, 591, L17
Suzuki, A., & Shigeyama, T. 2013, ApJ, 764, L12
Suwa, Y., & Ioka, K. 2011, ApJ, 726, 107
Toma, K., Ioka, K., Sakamoto, T., & Nakamura, T. 2007, ApJ, 659, 1420

van Leer, B. 1977, Journal of Computational Physics, 23, 276
Wang, X.-Y., Razzaque, S., & Mészáros, P. 2008, ApJ, 677, 432
Woosley, S. E. 1993, ApJ, 405, 273
Woosley, S. E., & Heger, A., 2006, ApJ, 637, 914
Yonetoku, D., Murakami, T., Nakamura, T., Yamazaki, R., Inoue, A. K., & Ioka, K. 2004, ApJ, 609, 935
Zhang, W., Woosley, S. E., & MacFadyen, A. I. 2003, ApJ, 586, 356
Zhang, W., Woosley, S. E., & Heger, A. 2004, ApJ, 608, 365